Lithos 378–379 (2020) 105831

Contents lists available at ScienceDirect

Lithos

journal homepage: www.elsevier.com/locate/lithos

Research Article

Geochemical evolution of the lithospheric mantle beneath the Styrian Basin (Western Pannonian Basin)

László Előd Aradi [a], Enikő Bali [b], Levente Patkó [a,c,1], Károly Hidas [d,2], István János Kovács [e], Alberto Zanetti [f], Carlos J. Garrido [d], Csaba Szabó [a,e,*]

[a] Lithosphere Fluid Research Laboratory, Department of Petrology and Geochemistry, Institute of Geography and Earth Sciences, Eötvös Loránd University, Budapest 1117, Hungary
[b] Nordic Volcanological Center, Institute of Earth Sciences, University of Iceland, Sturlugata 7, 101 Reykjavík, Iceland
[c] Institute for Nuclear Research, Isotope Climatology and Environmental Research Centre, Debrecen, Hungary
[d] Instituto Andaluz de Ciencias de la Tierra (IACT), Consejo Superior de Investigaciones Científicas (CSIC)-Universidad de Granada, 18100 Armilla, Granada, Spain
[e] Research Centre for Astronomy and Earth Sciences (CSFK), Geodetic and Geophysical Institute, Sopron 9400, Hungary
[f] Institute of Geosciences and Earth Resources, National Research Council of Italy (CNR-IGG), I-27100 Pavia, Italy

ARTICLE INFO

Article history:
Received 15 April 2020
Received in revised form 6 October 2020
Accepted 10 October 2020
Available online 14 October 2020

ABSTRACT

The Styrian Basin is located at the westernmost part of the Carpathian-Pannonian region, in the transition zone between the Pannonian Basin and the Eastern Alps. The lithospheric mantle beneath the Styrian Basin (SB) was sampled by Plio-Pleistocene alkali basalts, which brought mantle xenoliths to the surface. Mantle xenoliths from the SB are mostly coarse granular, amphibole-bearing spinel lherzolites with microstructures indicating extensive annealing. Three geochemical events were recorded in the SB xenoliths. The initial, ancient partial melting event was followed by an old metasomatism, which formed lithological heterogeneities (e.g. websterite, dunite) occurring as veins, bands and layers. The most recent geochemical event recorded in the SB xenoliths is the migration of a hydrous alkaline melt originating from a nephelinitic melt source. This melt migrated from the asthenosphere, forming melt channels in the lithospheric mantle. Close to the channels, the metasomatic agent caused extensive amphibole and sparse phlogopite formation. This particular pargasite-phlogopite equilibrium mineral assemblage in the spinel facies was not described before in the literature based on our knowledge. The reaction caused significant enrichment in basaltic elements (such as Ti, Fe), K, light rare earth elements and incompatible trace elements such as Zr and Hf. Further from the channels, the metasomatic melt became enriched in volatiles (mainly H_2O and CO_2) and fluid mobile elements (e.g. U, Pb, Cl and P), but depleted in basaltic elements, K and LREE, which resulted in modal decrease of amphiboles. Previous studies suggested a dehydrating subducted slab beneath the Styrian Basin, however geochemical fingerprints of subducted slab derived fluids were recognized only in one xenolith. Mantle portions with different geochemical characteristics developed in the lithosphere laterally, however metasomatic fingerprints were erased later due to annealing and chemical re-equilibration at ambient mantle conditions. The Neogene evolution of the lithosphere overwrote the previous state of the upper mantle beneath the region, thus the signs of the most recent metasomatism by nephelinitic melts could have been only preserved due to this extensive annealing event.

1. Introduction

To better understand the Neogene lithospheric evolution of the Carpathian-Pannonian region (CPR) numerous studies were performed on upper mantle xenoliths derived from volcanic fields (Fig. 1A) including the central parts (Bakony Balaton Highland and Little Hungarian Plain: e.g. Bali et al., 2007; Berkesi et al., 2012; Downes et al., 1992; Embey-Isztin et al., 2001; Hidas et al., 2010; Szabó et al., 1995), and the northern (Nógrád-Gömör: e.g. Liptai et al., 2017 and references therein), and eastern margins (Perşani Mountains) (e.g. Chalot-Prat and Boullier, 1997; Falus et al., 2008; Vaselli et al., 1995).

* Corresponding author at: Lithosphere Fluid Research Laboratory, Department of Petrology and Geochemistry, Institute of Geography and Earth Sciences, Eötvös Loránd University, Budapest 1117, Hungary.
E-mail addresses: aradi.laszloelod@ttk.elte.hu (L.E. Aradi), eniko@hi.is (E. Bali), levente.patko@ttk.elte.hu (L. Patkó), k.hidas@igme.es (K. Hidas), kovacs.istvan.janos@csfk.mta.hu (I.J. Kovács), zanetti@crystal.unipv.it (A. Zanetti), carlos.garrido@csic.es (C.J. Garrido), cszabo@elte.hu (C. Szabó).
[1] Currently: Research Centre for Astronomy and Earth Sciences (CSFK), Geodetic and Geophysical Institute, Sopron 9400, Hungary.
[2] Currently: Departamento de Investigación y Prospectiva Geocientífica, Instituto Geológico y Minero de España, Tres Cantos, Madrid, Spain; k.hidas@igme.es

https://doi.org/10.1016/j.lithos.2020.105831

Upper mantle derived xenoliths from the Styrian Basin (SB) were mentioned early (e.g. Heritsch, 1908) (Fig. 1B). Most papers focused on the best-known and studied localities in Kapfenstein and Tobaj (e.g. Coltorti et al., 2007; Dobosi et al., 1999, 2010; Kurat et al., 1980; Vaselli et al., 1996), despite the fact that numerous pyroclastic deposits and lava flows contain upper-mantle derived rock fragments (e.g. Bojar et al., 2013; Fig. 1B). From the deposit located in Slovenia (Grad) only petrographic data are published (Hinterlechner-Ravnik and Mišič, 1986). According to these studies, the lithospheric mantle beneath the SB is rather uniform both texturally and geochemically, thus it was used widely as a proxy for a primitive, undeformed subcontinental lithospheric mantle (SCLM). Coarse-grained, protogranular and porphyroclastic texture dominate the xenoliths that exhibit fertile geochemical characters. The studies also infer minor modal and cryptic metasomatism caused by CO_2-H_2O-rich mafic alkaline melts, based on the trace element geochemistry of clinopyroxenes and amphiboles (Coltorti et al., 2007; Dobosi et al., 1999, 2010; Vaselli et al., 1996). However, a recent petrographic and deformational study integrated with the structural hydroxyl content of nominally anhydrous minerals (NAMs) from new SB xenolith localities (Aradi et al., 2017) suggests that the lithospheric mantle is not homogeneous and is structurally complex under the SB. According to Aradi et al. (2017), the SCLM beneath the SB could have interacted with hydrous fluids resulting in extensive recrystallization and formation of hydrous minerals, which constrained the geochemical evolution of the Styrian Basin SCLM.

The goal of this study is to provide a detailed petrographic and geochemical database of upper mantle xenoliths of the SB. We report on samples from ten new localities, which were not studied previously. Our comprehensive geochemical dataset, combined with the previously published textural and microstructural data, and structural hydroxyl content, helps to reveal the evolution of the lithospheric mantle beneath the western edge of the Miocene Pannonian Basin. Due to the geodynamic situation of the Styrian Basin (i.e. in between the Alps and the central part of the Pannonian basin), this paper provides essential insight into physical and chemical processes of the lithospheric mantle, which could preserve fingerprints of different subduction phases and magmatic events during the Cenozoic. Additionally, a particular pargasite-phlogopite mineral assemblage is described, which testifies enrichment of the SCLM in both H_2O and K_2O in the spinel peridotite facies.

2. Geological background

The Carpathian-Pannonian region (CPR) is a young Miocene Mediterranean style extensional back-arc basin (e.g. Horváth et al., 2015), which is surrounded by the Bohemian Massif, the East European and Moesian Platform, the Dinarides, and the Alps, and the Carpathians (Fig. 1A, e.g. Csontos and Vörös, 2004; Fodor et al., 1999). It is composed of two major tectonic blocks: the ALCAPA (ALps-CArphathian PAnnonian) and the Tisza-Dacia, which are separated by the Mid-Hungarian Fault Zone (e.g. Bada and Horváth, 2001; Csontos and Vörös, 2004). The Styrian Basin is the westernmost sub-basin of the CPR (Ebner and Sachsenhofer, 1995), situated in the transitional zone between the Eastern Alps and the central part of the Pannonian Basin (Fig. 1A). The evolution of the SB is closely related to CPR geodynamics. The SB was developed above an Alpine lithospheric wedge (ALCAPA), which was displaced (from the late Oligocene to Early Miocene) eastwards ~450 km (e.g. Ebner and Sachsenhofer, 1995; Kázmér and Kovács, 1985; Ratschbacher et al., 1991). During the extrusion the lithosphere of the ALCAPA stretched and thinned, mainly in the central part

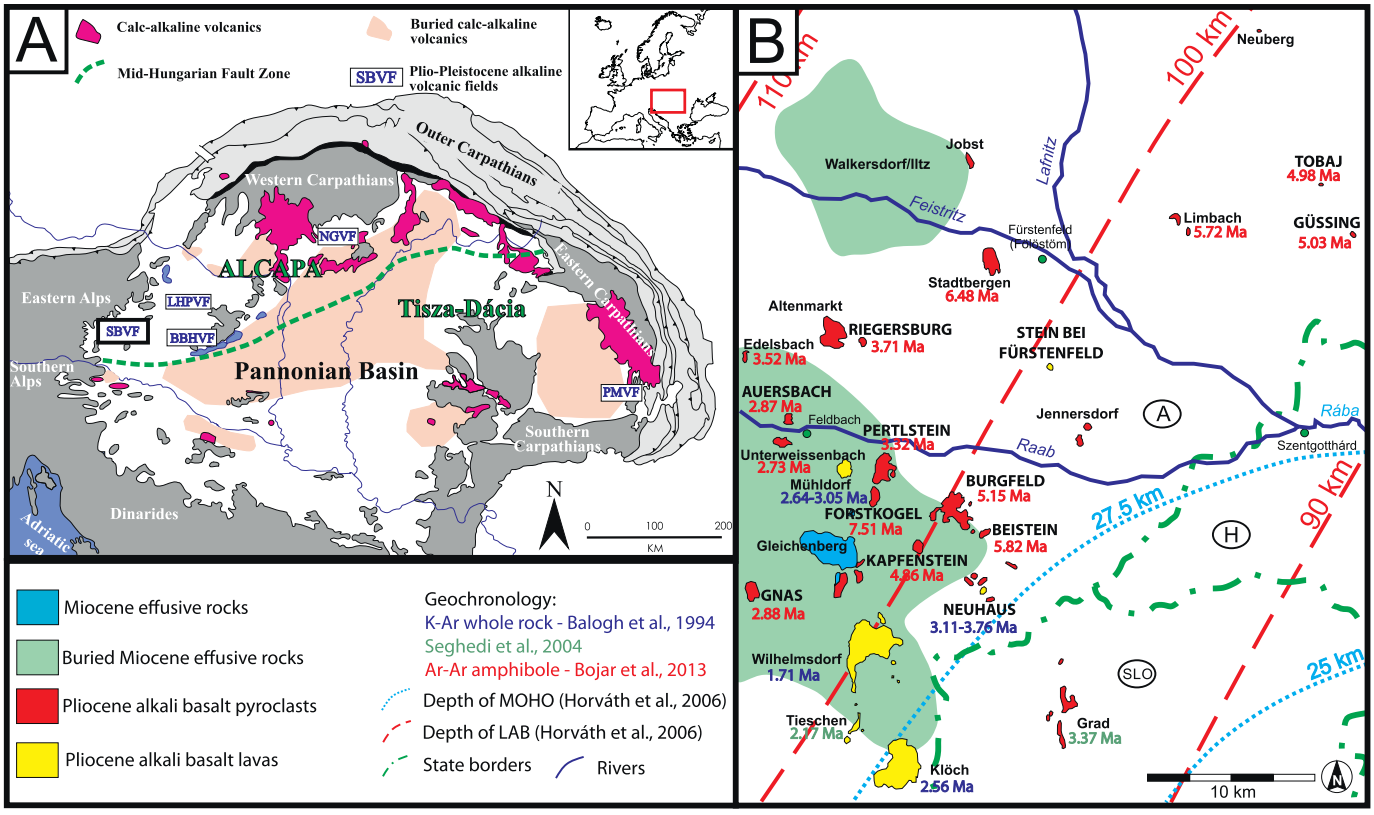

Fig. 1. A: Simplified tectonic map of the Carpathian-Pannonian region (CPR) and its surroundings (Harangi, 2001b; Szabó et al., 1992). Mantle xenolith-bearing alkaline basalts are present in the following volcanic fields: Styrian Basin Volcanic Field (SBVF); Little Hungarian Plain Volcanic Field (LHPVF); Bakony-Balaton Highland Volcanic Field (BBHVF); Nógrád-Gömör Volcanic Field (NGVF); Persani Mountains Volcanic Field (PMVF). The inset shows the location of the CPR in Europe. B: Simplified geological map of the Styrian Basin modified after Bojar et al. (2013).

(4–8 times in the central part, Huismans et al., 2001; Fig. 1A), but also affected the basin at the margins (e.g. Bada and Horváth, 2001), although less intensively (1.4–1.6 in the SB; Huismans et al., 2001). A SW oriented asthenospheric flow is suspected as the cause of the extrusion of the ALCAPA (Kovács et al., 2012), besides the collapse of the Alpine orogeny (Ratschbacher et al., 1991). The lithosphere-asthenosphere boundary (LAB) is at ~100 km depth, according to Horváth et al. (2006), and shows a small gradual thickening to the NW (Fig. 1B). More recent geophysical study by Bianchi et al. (2014) suggests significantly shallower LAB beneath the basin (60–80 km). The thickness of the crust is 27–30 km (Fig. 1B, Horváth et al., 2006). According to seismic tomographic models (e.g. Dando et al., 2011; Mitterbauer et al., 2011), evidence for a WSW-ENE oriented fast downwelling structure is observed in the upper mantle beneath the Styrian Basin. This anomaly could be related to the remnant of the detached Penninic slab (Mitterbauer et al., 2011; Qorbani et al., 2015) yielding an excellent study area for lithosphere evolution.

In Early to Middle Miocene times andesite to shoshonite magmas erupted in the south-eastern part of the Styrian Basin due to the ongoing extension and lithosphere thinning, which initiated melting in the metasomatized lithospheric mantle (Ebner and Sachsenhofer, 1995; Harangi, 2001a; Harangi et al., 1995). Based on the geochemistry of these volcanic rocks, a metasomatic event in the mantle could have happened above a subducted slab, probably during the Late Eocene subduction of the Penninic slab (Aradi et al., 2017; Harangi et al., 1995).

From the Late Miocene, the Pannonian Basin is in a compressional tectonic region, which leads to a tectonic inversion up until recent times (Fodor et al., 1999; Horváth et al., 2006). Due to this event, rapid and significant uplift affected the Styrian Basin (Ebner and Sachsenhofer, 1995). During this compressional phase from Miocene to Pleistocene times, the SB was the area of alkali basalt volcanic activity (Ali et al., 2013; Embey-Isztin et al., 1993; Heritsch, 1967). These post-extensional alkali basalts transported spinel peridotites and pyroxenites from the SCLM to the surface (e.g. Szabó et al., 2004). The alkali basalt volcanism was active from between 7.5 and 1.7 Ma with two significant episodes at 5.5–5 and 3–2.5 Ma (Fig. 1B; Balogh et al., 1994; Bojar et al., 2013; Pécskay et al., 2006). Their melts were generated by small volume (2–3%) decompression melting probably initiated by an upward asthenospheric flow (Embey-Isztin et al., 1993; Harangi et al., 2015).

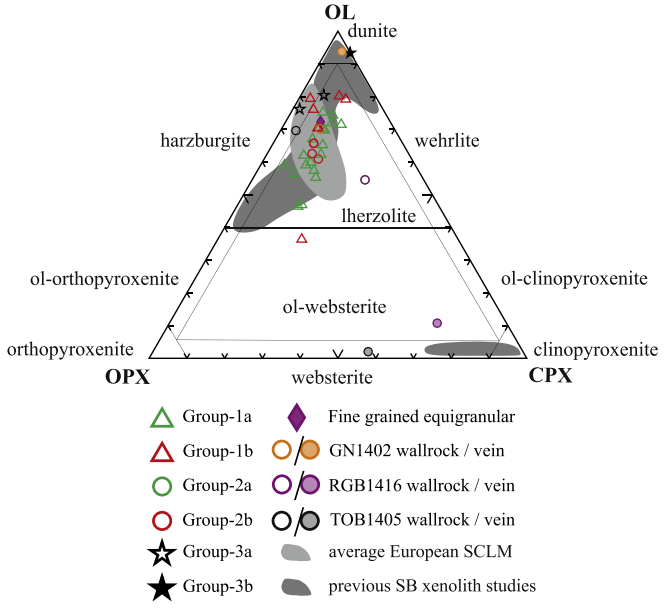

Fig. 2. Modal compositions of the studied Styrian Basin xenoliths in the system of Streckeisen (1976). Data of previous studies of Styrian Basin (SB) xenoliths is from Richter (1971), Kurat et al. (1980) and (1991) and Vaselli et al. (1996). Composition of the average European subcontinental lithospheric mantle (SCLM) is based on Downes (1999).

3. Sampling and analytical methods

Alkali basaltic volcanism can be found all across the Styrian Basin (Fig. 1B), where basaltic lava flows, tuffs and *syn*-eruptively reworked volcanoclastic deposits contain mantle xenoliths (e.g. Bojar et al., 2013 and references therein; Jugovics, 1915). We sampled 16 localities (Aradi et al., 2017) and collected >150 upper mantle xenoliths. From the localities of Limbach, Altenmarkt, Unterweissenbach and Grad, there were no xenoliths found to be suitable for a detailed petrographic and geochemical studies, mainly due to their size (<2 cm) or strong alteration. We selected 35 fresh xenoliths for detailed petrographic and geochemical study (Fig. 2, Table 1). These xenoliths are 3–30 cm in diameter. Only the xenoliths from Stein bei Fürstenfeld (SBF, Fig. 1B) are hosted in basalt lava, all the others are found in pyroclasts and other reworked volcaniclastic rocks. Often a thin (1–10 mm) glassy basalt rind covers xenoliths. Most xenolith are rectangular or slightly rounded in shape. We prepared 150–600 μm thick double polished sections from all selected xenoliths. These sections were used to carry out all petrographic and chemical analyses.

The major element analyses of the rock forming minerals were carried out using a CAMECA SX50 electron microprobe in Padua at CNR Institute for Geosciences and Earth Resources (IGG) and using a CAMECA SX100 electron microprobe at the Dionýz Štúr State Geological Institute, Bratislava. Both instruments operated with routine conditions of 15–20 kV accelerating voltage and 10–20 nA beam current. Counting times were 10 s at the peak and 5 s at the background for major elements and 20–40 s at peak and 10 s at the background for minor elements. Beam diameter varied between 3 and 10 μm. The detection limits of measured elements range from 0.02 to 0.1 wt%, and statistical errors from 0.02 to 0.1 wt% (1σ). The oxide weight percentages were gained from X-ray counts by using PAP correction program (Pouchou and Pichoir, 1991). Calibration on the SX50 was carried out based on the following standards: Si (jadeite), Ti (ilmenite), Al (plagioclase), Fe (ilmenite), Mn (rhodonite), Ni (nickel), Cr (chromite), Mg (olivine), Na (jadeite), K (sanidine). For the SX100, the following reference materials were used: Si (orthoclase), Ti (TiO_2), Al (Al_2O_3), Fe (fayalite), Mn (rhodonite), Cr (chromite), Ni (nickel), Zn (willemite), V (vanadium), Ca (wollastonite), Mg (MgO), Na (albite), K (ortoclase), F (LiF), Cl (NaCl).

Trace element analyses of ortho-, clinopyroxene, amphibole and mica were performed by LA-ICP-MS at Institute of Geosciences and Earth Resources, C.N.R., Pavia, Italy, using a Perkin Elmer ELAN DRC-e quadrupole mass spectrometer coupled with a Q-switched Nd:YAG laser source Brilliant (Quantel, Les Ulis, France). The laser was operated at a repetition rate of 10 Hz, with a pulse energy of ~35 mJ. Helium was used as carrier gas and was mixed with Ar downstream of the ablation cell. Spot diameter was adjusted in the range of 40–100 μm. Data reduction was performed offline using the GLITTER software. Precision and accuracy of the trace element concentrations were assessed through repeated analysis of the BCR2-g standard to be better than ±7% and ± 10%, respectively, at the ppm concentration level (for further details see Miller et al., 2012). NIST SRM 610 synthetic glass standard was used as external standard and CaO was used as internal standard for clinopyroxene and amphibole, whereas SiO_2 was used for orthopyroxene and phlogopite.

Complementary measurements on the heterogeneous clinopyroxenes were carried out at the Andalchron analytical facilities of the IACT (CSIC, Armilla, Granada, Spain) using of Photon Machines Excimer 193 nm wavelength Laser (G2-Analyte Excite) technique attached to an Agilent 8800 ICP-MS/MS. The laser acquisition parameters were: ~12 J/cm^2 energy density, 10 Hz repetition rate and 40–100 μm spot size. The primary calibration standard was the NIST612 synthetic glass (Pearce et al., 1997). The internal standard was CaO for the clinopyroxenes.

Table 1.
Summary table of the main petrographic and geochemical properties of the studied Styrian Basin xenoliths. Degree of melting is calculated based on Hellebrand et al., 2001. Negative values were omitted (n.d.) Abbreviations: ol – olivine; opx – orthopyroxene; cpx – clinopyroxene; spl – spinel; amp – amphibole; phl – phlogopite; ap – apatite; lhz – lherzolite; hzb – harzburgite; wht – wehrlite; wbs – websterite; prot - protogranular; porph – porphyroclastic; fg eq - fine grained equigranular; Fo - forsterite content of olivine. Equilibrium temperature calculations were based on Brey and Köhler, 1990; T_{BK}), also modified by Nimis and Gütter, 2010 (T_{NG}); Witt-Eickschen and Seck (1991, T_{WES}) and Liang et al. (2013; T_{REE}).

Xenolith	Locality	Lithology	Group	Ol	Opx	Cpx	Spl	Amp	Phl	Ap	T_{BK}	T_{NG}	T_{WES}	T_{REE}	T_{BK} - T_{REE}	Fo	Sp Cr#	Degree of melting (%)	La_N/Lu_N in cpx	Y_N
AUB1407	Auersbach	prot lhz	1a	68	18	11	2.5	0.24			1049	975	979	1032 ± 36	17	89.5	9.1	46.14	0.38	4.0
AUB1410		prot lhz	1a	58	26	13	2.3	0.08			1038	972	1014	1007 ± 25	31	90.5	11.5	48.39	0.36	3.9
BEI1401	Beistein	ol-wbs	1b	34	39	21	1.6	2.46			1022	999	958	1053 ± 46	-32	90.0	8.8	n.d.	5.70	3.6
BEI1402		prot lhz	1a	45	36	16	3.5	n.d.			1056	993	979	1065 ± 6	-9	89.3	9.3	46.29	0.58	4.3
BEI1403		phl-bearing wht	3b	63	n.d.	5	n.d.	32.4	+		n.a	n.a	n.a	n.a	n.a	85.6	63.9	65.58	7.33	4.2
BEI1404		prot lhz	1a	69	18	12	1.2	n.d.			951	908	996	1044 ± 13	−93	90.2	12.0	48.85	0.45	4.0
BF1411	Burgfeld	phl-bearing hzb	3a	68	11	5	0.0	15.94	+	+	968	937	793	1020 ± 78	−52	88.2	51.6	63.44	11.96	5.1
FKG1402	Forstkogel	prot lhz	2b	60	24	14	0.3	0.45			988	978	966	986 ± 40	2	88.6	9.4	46.42	3.12	4.1
GN1401	Gnas	porph lhz	1b	68	19	10	0.9	2.04			896	912	949	939 ± 8	−42	90.4	17.9	52.86	8.13	2.2
GN1402		porph lhz	2b	61	25	12	2.2	n.d.			944	915	954	1018 ± 0	−73	90.1	20.8	54.36	3.63	2.4
		dunite vein		90	2	4	3.3	1.17			n.a	n.a	n.a	n.a	n.a	n.a	n.a	n.a	n.a	n.a
GN1406		prot lhz	1a	60	23	14	2.3	0.44			956	939	944	1036 ± 31	−80	90.2	11.5	48.46	0.30	3.7
GN1407		phl-bearing hzb	3a	66	19	2	0.1	13.21	+	+	1029	942	763	n.a	n.a.	90.4	51.5	63.41	n.a.	n.a.
GN1411		porph lhz	1b	75	18	6	0.9	0.92			906	939	927	960 ± 24	−54	90.4	22.4	55.08	13.00	2.2
GN1412		porph lhz	1a	71	15	12	1.4	0.01			973	944	965	957 ± 8	15	90.1	10.9	47.86	0.21	4.5
GS0611	Güssing	fg eq lhz		71	18	9	1.1	0.01			770	801	822	1476 ± 217	−706	90.2	26.2	56.67	1.76	0.3
GS1408		porph lhz	1a	58	34	6	2.1	0.01			911	894	967	971 ± 31	−60	91.1	19.3	53.58	0.42	3.8
KPFS0402	Kapfenstein	prot lhz	1a	46	35	17	1.2	0.19			1053	1007	1018	1035 ± 9	18	90.1	11.9	48.73	0.63	3.8
KPFS0404		prot lhz	1a	73	14	12	1.2	0.17			1027	976	985	1029 ± 19	−2	89.9	11.2	48.16	0.30	3.5
KPFS0420		prot lhz	1a	70	13	15	1.4	0.04			1054	986	1014	1062 ± 9	−8	89.8	9.8	46.82	0.28	3.2
KPFS0421		prot lhz	1a	55	33	10	2.1	n.d.			1047	983	1006	1016 ± 21	31	89.9	14.8	50.94	0.28	3.4
NH0601A	Neuhaus am	porph lhz	1a	66	23	10	1.1	n.d.			860	919	1007	921 ± 52	−60	90.2	16.4	51.95	0.61	3.7
NH0602B	Klausenbach	porph lhz	1a	61	28	10	1.5	0.5			1083	929	902	937 ± 6	146	89.1	9.6	46.63	0.29	4.9
NH1402		porph lhz	1a	53	27	16	3.2	0.08			967	909	983	1039 ± 1	−71	89.7	9.5	46.50	0.15	4.3
NH1408		porph lhz	1b	70	20	10	0.7	0.05			950	895	960	962 ± 82	−12	90.6	15.4	51.37	3.58	3.7
PST1401	Pertlstein	prot lhz	1a	58	29	12	0.9	0.01			985	976	1047	1186 ± 14	−201	90.4	17.2	52.43	0.72	3.5
PST1403		porph lhz	1a	63	21	13	3.1	0.02			964	953	1003	1028 ± 14	−64	90.5	17.8	52.78	0.81	3.2
RGB1415	Riegersburg	porph lhz	1b	78	8	13	0.1	1.76			1093	966	897	1064 ± 103	28	89.8	51.8	63.48	6.82	3.1
RGB1416		prot lhz	2a	62	19	18	0.9	0.30			941	954	958	1012 ± 24	−71	89.4	9.0	n.d.	0.12	3.7
		ol-wbs layer		9	18	70	2.0	1.00			n.a	n.a	n.a	n.a	n.a	n.a	n.a	n.a	n.a	n.a
RGB1454		porph lhz	2b	59	24	11	0.6	4.58			960	960	940	938 ± 6	22	89.7	14.8	50.91	4.71	4.2
RGB1456		sheared lhz	2b	63	22	11	0.9	3.38			1053	985	990	1036 ± 3	17	89.4	19.5	53.70	0.24	3.9
SBF1401	Stein bei Fürstenfeld	porph lhz	1a	74	16	8	2.0	0.07			888	914	1007	915 ± 6	−26	90.5	15.6	51.47	0.51	3.2
TOB1401	Tobaj	porph lhz	1a	56	27	15	2.1	0.53			1028	966	943	1103 ± 63	−74	90.2	11.2	48.17	0.43	3.9
TOB1402		porph hzb	1b	79	17	3	0.5	n.d.			1089	1056	1053	1089 ± 46	−1	89.7	26.3	56.69	2.26	2.3
TOB1403		prot lhz	1b	72	8	9	1.1	8.65			1013	1031	949	1114 ± 17	−102	88.8	15.8	51.59	3.45	3.4
TOB1405		phl-bearing prot hzb	3b	50	19	3	4.5	5.65	+		950	948	993	944 ± 21	6	86.3	15.5	51.44	0.53	4.8
		wbs vein		n.d.	40	55	5.3	n.d.			941	930	947	1010 ± 60	−69	n.a.	n.a.	n.a.	0.31	5.9

For quality control, we analyzed the BIR-1G and BHVO-2G reference glasses (Jochum et al., 2005) as secondary standards. Data processing was carried out using Iolite 2.5 software (Paton et al., 2011). Data comparison between the clinopyroxenes measured at both institutions can be found in Supplementary Text 1.

Micro-Raman spectroscopic analysis was done to determine the composition of apatite at the Research and Industrial Relations Center of the Faculty of Science, Eötvös University, Budapest, using a HORIBA Labram HR800 spectrometer with Nd:YAG laser ($\lambda = 532$ nm). The details of the used analytical methods are described in more details in Supplementary Text 1.

4. Petrography

The detailed petrographic features for most of our Styrian Basin xenoliths are reported in Aradi et al. (2017). Here, we summarize the typical petrographic characteristics of the xenoliths and provide more details about features connected to mineral reactions at mantle conditions and textures associated with metasomatic processes. We divided the xenoliths into three groups based on their lithology and texture.

Group-1 xenoliths have coarse grained (average grain size between 1500 and 3000 μm) protogranular and porphyroclastic textures (Fig. 3A, Aradi et al., 2017). Based on their modal compositions, most of them are amphibole-bearing lherzolites (30 out of 35; Fig. 2). Amphibole usually appears as a rim on clinopyroxenes and spinels (Fig. 3B).

Group-2 xenoliths show the same petrographic textures as Group-1 xenoliths, however they display lithological heterogeneities in the forms of veins, monomineralic layers or bands (e.g. Fig. 3C and D). Veins vary in thickness from 0.2–0.5 mm (Fig. 3C) up to 1–5 mm (Fig. 3D). Bands have diffuse border with the wall rock and occur for example as 2.5 cm thick dunite (Fig. 3D). Group-2 lherzolite RGB1456 (Fig. S1) has a sheared, amphibole-bearing zone, described in detail in Supplementary Text 2.

Group-3 xenoliths make up four amphibole-rich (> 5 vol%) peridotites, in which phlogopite was also identified. Phlogopite was previously found in a hornblendite from Kapfenstein (Kurat et al., 1980) and in clinopyroxenite from Tobaj (Richter, 1971). Phlogopite is always included in amphibole (Fig. 4B, D and E), forming single crystal flakes or small clusters with grain size ranging between 100 and 500 μm (Fig. 4E). In the core of phlogopites vermicular spinels were found

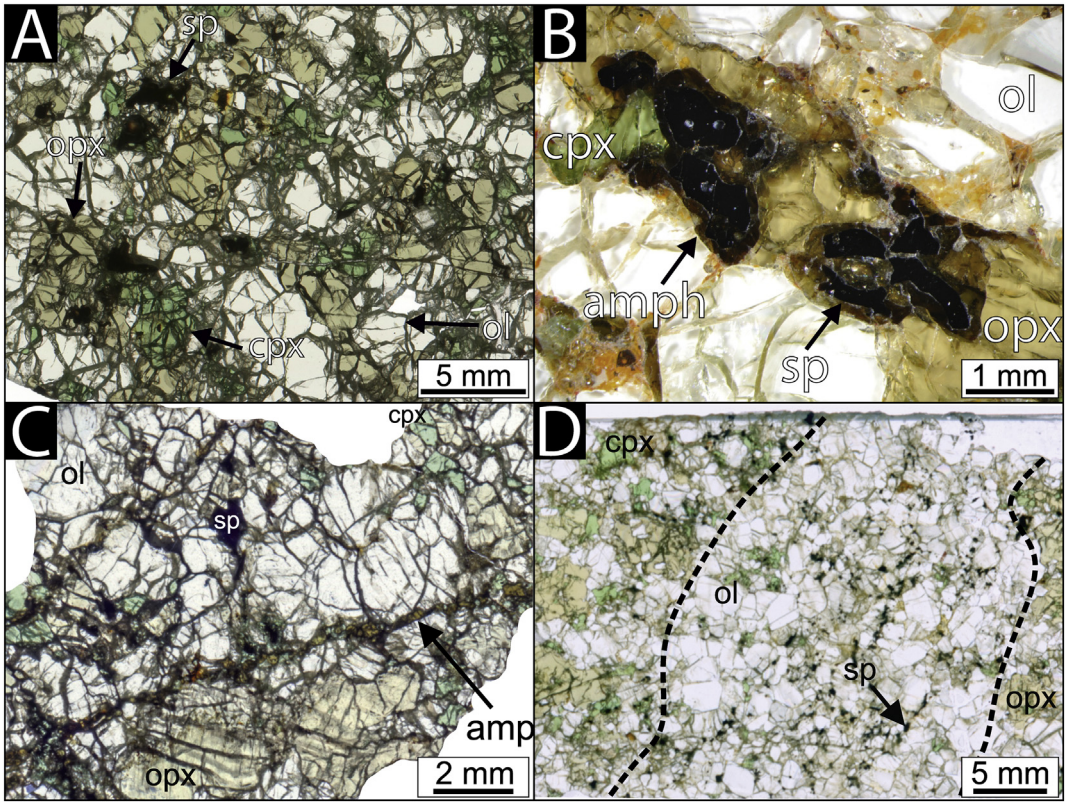

Fig. 3. Petrography of the Group-1 and Group-2 xenoliths of the Styrian Basin. A: Representative texture of the protogranular Group-1a AUB1410 lherzolite. Transmitted light, 1 N. B: Amphibole occurring at the contact of pyroxenes and spinels in the protogranular Group-1b lherzolite TOB1403. Stereomicroscope image. C: Porphyroclastic texture of the Group-2b RGB1454 lherzolite. Thin amphibole vein crosscuts the lherzolite xenolith. Scanned image. D: Porphyroclastic texture of the Group-2b GN1402 lherzolite. The black dashed curves denote the contact of the dunite band and the wall rock lherzolite. Abbreviations: ol – olivine; opx – orthopyroxene; cpx – clinopyroxene; sp – spinel; amp – amphibole.

(Fig. 4D and E). Amphiboles appear in two textural positions: I) forming millimeter sized pockets by subhedral amphibole grains (Fig. 4A and E), often with a vermicular spinel in the core, and II) replacing ortho- and clinopyroxenes with thin (1–10 μm) lamellae (Fig. 4F) in the core of the pyroxenes and as rims around them. These pyroxenes are recrystallized partially into euhedral or flame-like patchwork structured amphiboles (Fig. 4C). Apatite is an accessory mineral in BF1411 and GN1407 harzburgites (subdivided into Group-3a), only 1–3 grains can be found per thin section. They appear mostly as rounded, 30–150 μm subhedral inclusions in amphibole and clinopyroxene partially replaced by amphibole (Fig. 4F). The phlogopite-bearing xenoliths, containing no apatite, were subdivided into Group-3b. Harzburgite TOB1405 contains a 0.5–1 cm thick pyroxenite vein (Fig. S2), but the petrographic positions of the phlogopites and amphiboles are the same as in Group-3 xenoliths (Supplementary Text 2).

Lherzolite GS0611 (Fig. S3) is the only fine grained equigranular (average grainsize ~850 μm) xenolith in the studied suite. Its detailed petrographic description is found in Aradi et al. (2017) and in the Supplementary Text 2.

5. Mineral geochemistry

5.1. Major elements

The forsterite content (Fo = Mg/Mg + Fe_{total} cationic ratios) of the analyzed olivines range between 0.88 and 0.91 (Fig. 5A; Table S1), except in the Group-3b xenoliths, where Fo is 0.86. The NiO content varies between 0.20 and 0.48 wt% (Fig. 5A). Olivines of the Group-3a GN1407 harzburgite deviate from the variation displayed by the other xenoliths since the highly magnesian olivines (Fo ~ 0.91) have low NiO contents (<0.3 wt%) (Fig. 5A). MnO contents vary from 0.12 to 0.29 wt%. The CaO concentrations are between 0.03 and 0.10 wt%, except in the fine grained equigranular lherzolite GS0611, in which CaO is below the detection limit (0.02 wt%), whereas in the Group-3b wehrlite BEI1403 it is above 0.12 wt%.

The orthopyroxene Mg# ($Mg\#_{OPX}$ = Mg/Mg + Fe_{total} cationic ratios) vary between 88 and 92 (Fig. 5B, Table S2). The Al_2O_3 in the orthopyroxenes is between 1.37 and 5.24 wt% (Fig. 5B), their CaO content is below 0.9 wt% (Table S2). In the Group-3a harzburgites, the orthopyroxenes, which are transformed partially into amphiboles, have the lowest Al_2O_3 (< 2 wt%; Fig. 5B). In the orthopyroxenes of the equigranular GS0611 xenolith the Al_2O_3 content is also remarkably low (2.16 wt%, Fig. 5B).

The Mg# of clinopyroxenes ($Mg\#_{CPX}$ = Mg/Mg + Fe_{total} cationic ratios) ranges between 88 and 92 (Table S3), except in the equigranular GS0611 ($Mg\#_{CPX}$ = 94) and in the Group-3b xenoliths ($Mg\#_{CPX}$ < 87). Their Na_2O and TiO_2 contents are between 0.85 and 1.82 and 0.12 and 0.89 wt%, respectively. In the Group-1 and Group-2 xenoliths, the clinopyroxenes have higher Al_2O_3 content than in Group-3 xenoliths, except TOB1405, in which clinopyroxenes are similar to those in Group-1 and Group-2 (Fig. 5C). The Group-3b wehrlite BEI1403 have clinopyroxene with higher TiO_2/Al_2O_3 ratio compared to all the SB xenolith suite (Fig. 5D). Concentration of Al_2O_3 in clinopyroxenes are always higher than in orthopyroxenes, except in the equigranular lherzolite GS0611. Its clinopyroxenes have the lowest Al_2O_3, Na_2O and TiO_2 concentrations coupled with exceptionally high CaO content (above 24 wt%, Table S3).

The Cr# (Cr# = $Cr^{3+}/Cr^{3+}+Al^{3+}$ cationic ratios, 9–52) and Mg# ($Mg\#_{SP}$ = Mg/Mg + Fe^{2+} cationic ratios, 45–88) number of the spinels show large variability (Fig. 6A, Table S4). In the Group-3 xenoliths, the

spinels show lower Mg# and higher Cr# compared to those in Group-1 and Group-2 xenoliths, except in Group-3b harzburgite TOB1405 (Fig. 6A). The #Mg and Cr# of spinels in this xenolith resemble the ones of Group-1 and 2. Compared to these two groups, enrichment in TiO_2 and FeO is observed in spinels from the matrix of the Group-2 sheared lherzolite RGB1456 and in Group-3b wehrlite BEI1403 (Table S4). All the studied xenoliths, except the Group-3a harzburgite BF1411 and Group-3b xenoliths plot within the OSMA-field (Olivine-Spinel Mantle Array, Fig. 7; Arai, 1987).

Amphiboles are mainly pargasites and magnesio-hastingsites in the studied xenoliths (Table S5; Hawthorne et al., 2012) and show a significant variation in major element composition. Amphiboles in Group-1 and Group-2 xenoliths have higher Na_2O, FeO, Al_2O_3 and lower K_2O, TiO_2 compared to those in Group-3 xenoliths (Fig. 6B and C). The highest K_2O contents (≥1 wt%) were measured in the xenoliths where the modal amount of amphibole is also the highest (Fig. 6D; Table 1). In Group-1 and Group-2 amphiboles show enrichment in K_2O (up to 1 wt%) without significant change in FeO content. On the other hand, amphiboles in Group-3b xenoliths show stronger enrichment in K_2O, which is also associated with elevated FeO content (Fig. 6B).

Based on the major elements, the micas are phlogopites, their Mg# range between 81 and 91 and show positive correlation with Al_2O_3 and Cr_2O_3 and negative correlation with TiO_2 content (Fig. 6E). Phlogopites in Group-3b xenoliths are more enriched in FeO, TiO_2 and more depleted in Al_2O_3 compared to those in Group-3a xenoliths. Fluorine content of the phlogopites is up to 0.9 wt%, Cl ranges from 0.01 to 0.18 wt% (Table S6). The phlogopites have Mg# and concentration of TiO_2, K_2O and Cr_2O_3 similar to amphiboles that enclosed them (Table S5 and S6).

Apatites were found in only Group-3a harzburgites BF1411 and GN1407 with SrO content around 1 wt% (Table S7). The apatites are Cl-rich (>1.8 wt%), F is below detection limit. The apatite in harzburgite GN1407 is richer in SO_3 (>0.5 wt%) than in harzburgite BF1411 (~0.1 wt%). As additional anion, CO_3^{2-} was detected with Raman spectroscopy. Raman bands of carbonate ions in the apatites were detected at ~1021, ~1042 and ~ 1070 cm^{-1} (Awonusi et al., 2007; Fig. S4).

To conclude, the comparison of our dataset with previously published major element data on SB xenoliths (Figs. 5 and 6) reveals that most Group-1 and Group-2 xenoliths overlap with previously published data. However, Group-3 and the fine grained equigranular xenolith could represent mantle domains not described before in the SB.

5.2. Mineral major element heterogeneities

Considerable major element inhomogeneity in minerals was observed in the Group-2 sheared lherzolite RGB1456 (Fig. S1). The silicates in the fine grained matrix display slightly lower Fo (e.g. Fo =88.5) and Na_2O in clinopyroxene (1.22 wt%) than their porphyroclastic counterparts (Fo = 89.5; Na_2O_{CPX} = 2.07 wt%). In the matrix, relict spinels, surrounded by amphiboles, are richer in Cr than the larger ones in

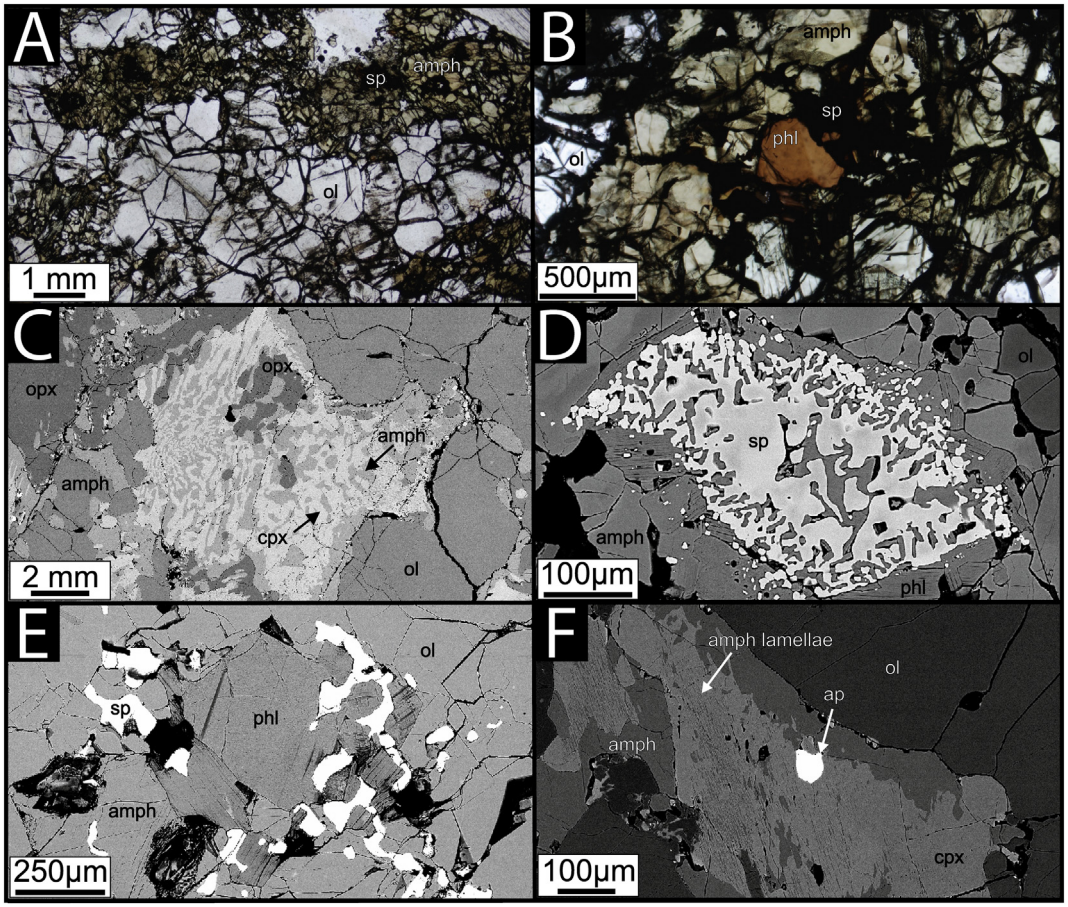

Fig. 4. Petrography of the Group-3 Styrian Basin xenoliths. A: Texture of the GN1407 harzburgite. 1 N, transmitted light. B: Phlogopite and vermicular spinel as inclusions in amphibole from the GN1407 lherzolite. 1 N, transmitted light. C: Backscattered electron image of an amphibole-orthopyroxene-clinopyroxene assemblage in the BF1411 harzburgite. D: Backscattered electron image of a spinel remnant surrounded by a thin phlogopite, and a thicker amphibole crystal from the TOB1405 lherzolite. E: Backscattered electron image of a phlogopite inclusion and spinel grain in amphibole, from the GN1407 harzburgite. F: Amphibole lamellae and rim on a clinopyroxene from the BF1411 harzburgite. Apatite is included in the clinopyroxene remnant. BSE image. Abbreviations: ol – olivine; opx – orthopyroxene; cpx – clinopyroxene; sp. – spinel; amp – amphibole; phl – phlogopite.

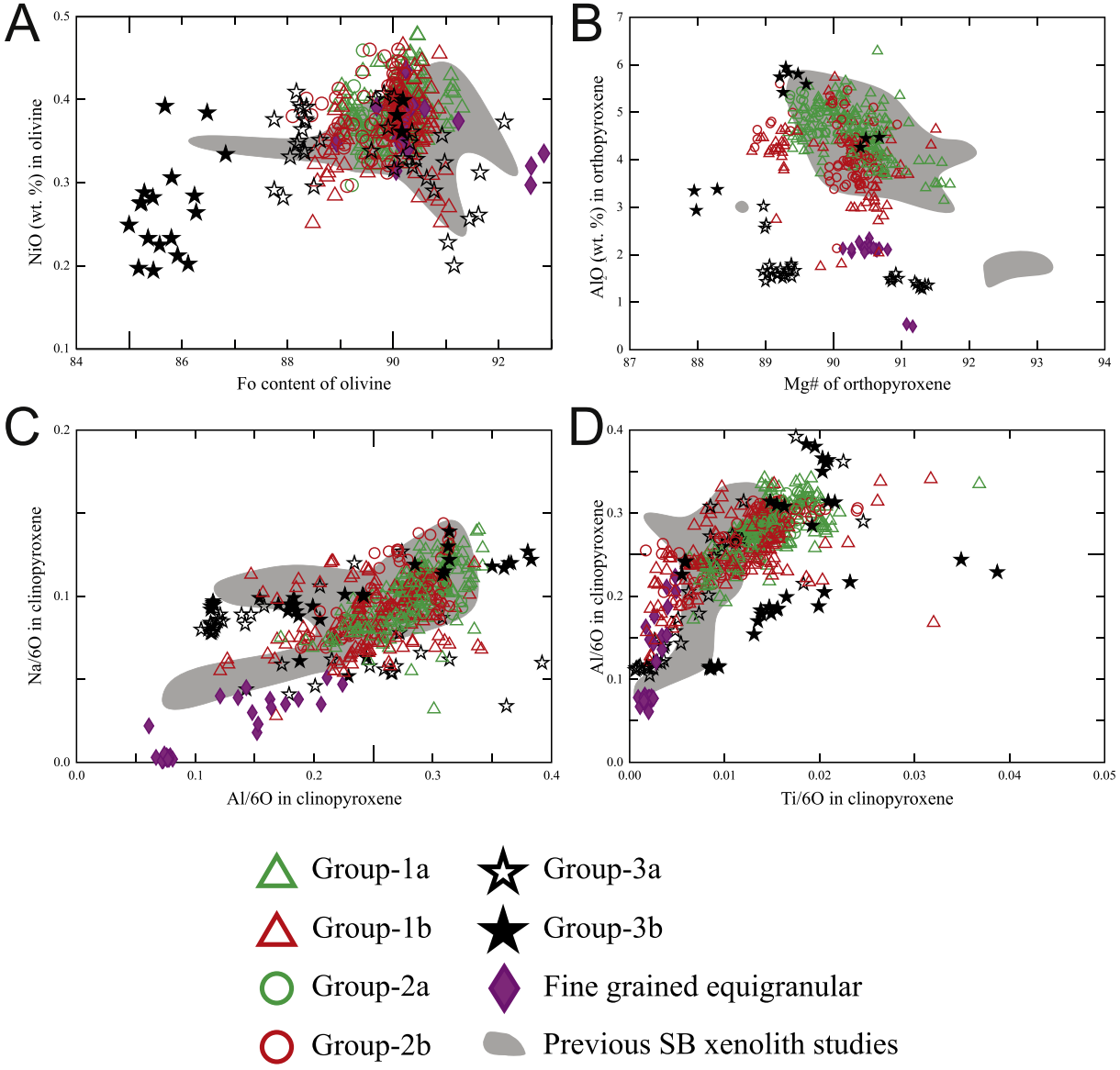

Fig. 5. Scatter plots of the major element content of the rock-forming silicates in Styrian Basin xenoliths. A: Forsterite (Fo, $Mg^{2+}/(Mg^{2+}+Fe^{2+})$) vs. NiO (wt%) in olivine. B: Mg# ($Mg/(Mg + Fe^{2+})$) vs. Al_2O_3 (wt%) in orthopyroxene. C: Cation numbers of Al vs. Na in clinopyroxenes. D: Cation numbers of Al vs. Ti in clinopyroxenes. Data of previous studies of Styrian Basin xenoliths are from Richter (1971), Kurat et al. (1980, 1991), Vaselli et al. (1996), Dobosi et al. (1999) and Coltorti et al. (2007).

the undeformed section of the xenolith (Cr_2O_3 = 47 and 11 wt%, respectively).

Centimeter-scale major element heterogeneity was also observed in the petrographically complex and heterogeneous Group-3b xenolith TOB1405 (Fig. S2): the rock-forming minerals in the harzburgite wall rock (closer to the amphibole-phlogopite clusters) display lower Mg content (e.g. Fo ≈ 86) than those further away from them (Fo ≈ 90). The resorbed spinels with phlogopite and amphibole rims also display higher #Cr than the intact ones (~0.4 and ~ 0.15, respectively). Sodium in clinopyroxene is similar in the wall-rock and in the pyroxenite vein (~1.8 wt%), however in the spongy clinopyroxenes near the wall rock-vein (Fig. S2A) contact Na_2O is slightly lower (~1.3 wt%).

5.3. Trace elements

5.3.1. Clinopyroxene

Incompatible trace elements in clinopyroxene (Table S8) vary over up to 3 orders of magnitude. Based on trace element characteristicsin Group-1 and Group-2 xenoliths, two subgroups (a and b) are distinguished.

In subgroups 1a and 2a, the clinopyroxenes display a LREE depleted, flat normalized pattern from Sm to Lu (Fig. 8A) with $(La/Lu)_N$ between 0.12 and 0.81 and are enriched in HREE compared to both the CI carbonaceous chondrite ($Yb_N > 3$; McDonough and Sun, 1995) and the Primitive Mantle (PM, McDonough and Sun, 1995). Clinopyroxenes in these groups are depleted in LILE and HFSE compared to the PM (Fig. 8B). The only exceptions are those from Group-1a lherzolites BEI1404 and KPFS0402, which show 2–4 × PM and 3–5 × PM enrichment in U and Th, respectively.

Clinopyroxenes in Group-1b and Group-2b xenoliths show more variable LREE patterns compared to those in the Group-1a and Group-2a xenoliths. In these subgroups, the clinopyroxenes have higher $(La/Lu)_N$ than 1, but lower HREE contents ($Yb_N < 3$) compared to the Group-1a and Group-2a xenoliths (Fig. 8C). Clinopyroxenes in some Group-1b and Group-2b xenoliths have a flat REE patterns from Nd to Lu, but show enrichment in La and Ce ($(La/Lu)_N > 2.5$). These clinopyroxenes also have the lowest negative Nb, and smallest negative Sr anomalies of Group-1b and Group-2b xenoliths exhibiting depletion in Zr and Hf, and the highest U and Th concentrations (Fig. 8D). Two

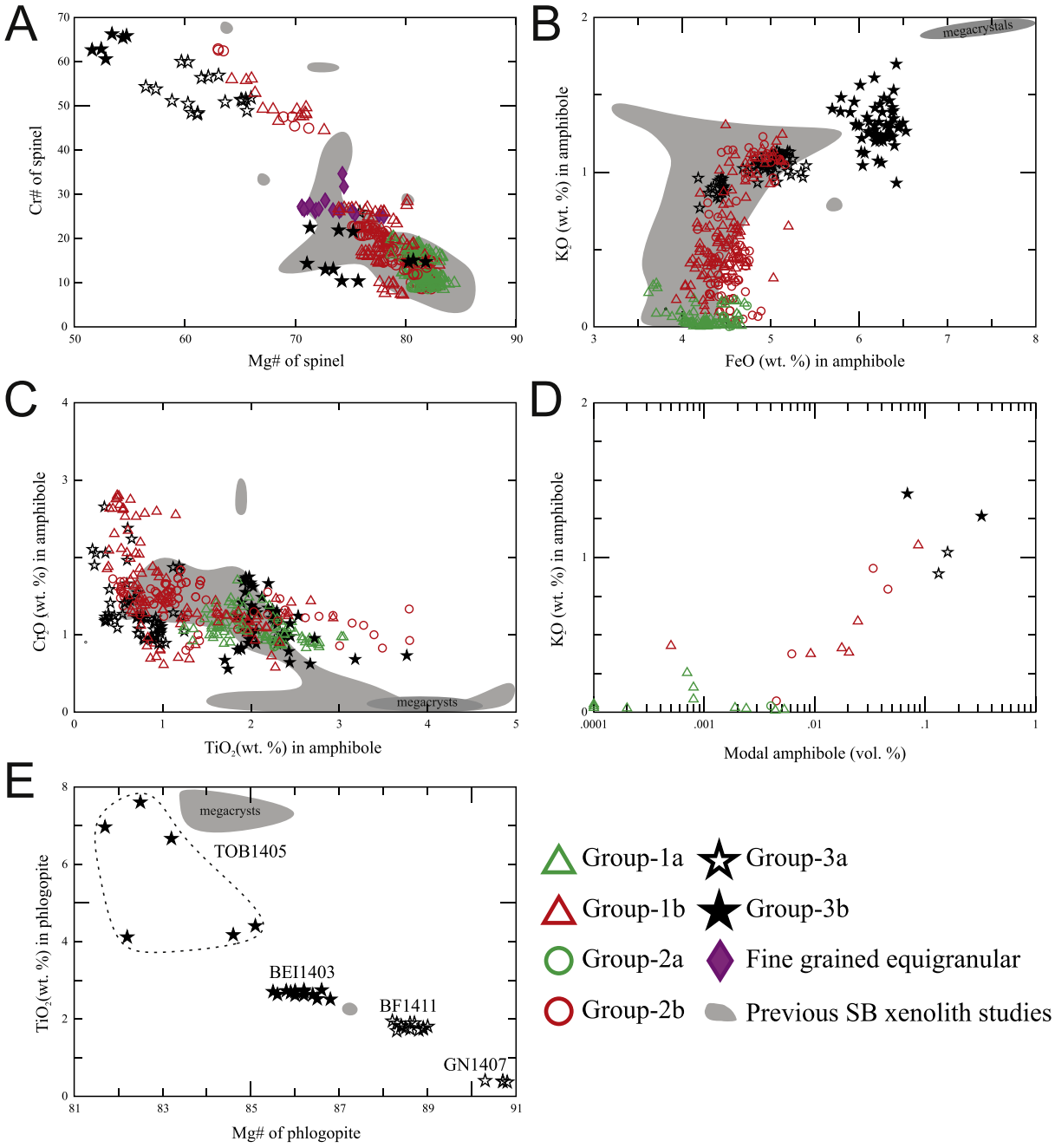

Fig. 6. Scatter plots of the major element content of the rock-forming minerals in Styrian Basin xenoliths. A: Mg# ($Mg/(Mg + Fe^{2+})$) vs. Cr# ($Cr^{3+}/(Cr^{3+}+Al^{3+})$) of spinel. B: FeO (wt%) vs. K_2O (wt%) of amphiboles. C: TiO_2 (wt%) vs. Cr_2O_3 (wt%) of amphiboles. D: Variation of K_2O (wt%) in amphiboles as a function of their modal abundance in the studied Styrian Basin xenoliths. E: Mg# ($Mg/(Mg + \Sigma Fe)$) vs. TiO_2 (wt%) of phlogopites. Data of previous studies of Styrian Basin xenoliths is from Kubovics et al. (1989), Kurat et al. (1980, 1991), Vaselli et al. (1996), Dobosi et al. (1999) and Coltorti et al. (2007).

xenoliths from Group-1b show flat distribution throughout the REY spectrum.

Clinopyroxenes in the Group-3b wehrlite BEI1403 and in the Group-3a harzburgite BF1411 have highly elevated REY content and show concave upward patterns starting from Ce to Dy, with a small dip at La (Fig. 8E). These clinopyroxenes display negative Zr, Hf and Pb anomalies (Fig. 8F). Furthermore, clinopyroxene of the Group-3a harzburgite BF1411 is more enriched in LILE elements and Nb and Ta, and overall in all trace elements compared to clinopyroxenes in wehrlite BEI1403. In the Group-3b lherzolite TOB1405 (Fig. S2) all the measured clinopyroxenes have a particular REY pattern (Fig. S11 and S12). Clinopyroxene in the pyroxenite vein (Fig. S11D and E) and in the harzburgite wall rock (Fig. S11A) show patterns similar to Group-1a and Group-2a xenoliths. The pyroxenes close to the pyroxenite vein (Fig. S11B and C) show flat, LREE depleted patterns, in one grain with a slight positive anomaly in Eu and Gd (Fig. S11B). Another grain neighboring spongy orthopyroxene shows flat REY pattern with a maximum at Nd (Fig. S11F).

The equigranular lherzolite GS0611 has a specific, U-shaped chondrite normalized REY-pattern, with near chondritic REY concentrations and a slight negative anomaly of Eu (Fig. 8G). Normalized to the PM, clinopyroxene in GS0611 xenolith is depleted in all the incompatible elements, except U, Sr and Pb. The latter has a significant positive anomaly compared to Ce and Pr (Fig. 8H).

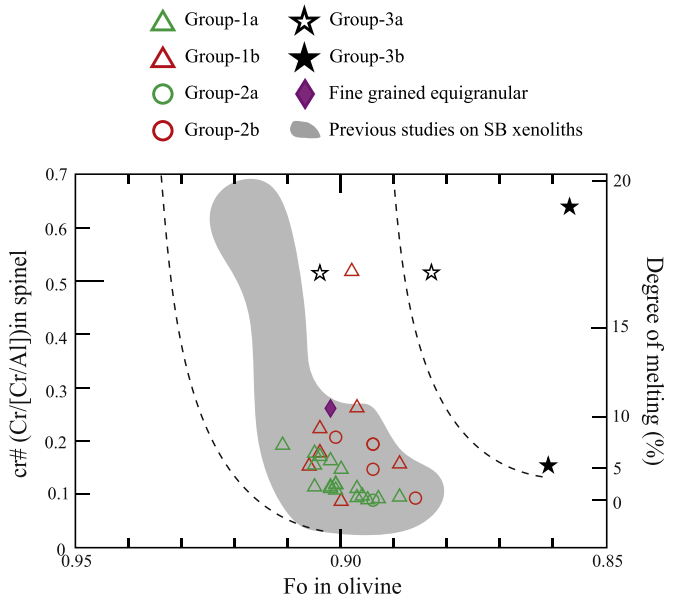

Fig. 7. OSMA (Olivine-Spinel Mantle Array; Arai, 1987) diagram of Cr# ($Cr^{3+}/(Cr^{3+}+Al^{3+})$) of spinel vs. forsterite content (Fo; $Mg/(Mg + Fe^{2+})$) of olivine in Styrian Basin xenoliths. Data from previous studies (Coltorti et al., 2007; Dobosi et al., 1999; Kurat et al., 1980, 1991; Vaselli et al., 1996) cover the grey field. Degree of melting was calculated by the equation of Hellebrand et al. (2001.)

Few xenoliths exhibit chemical heterogeneity in their clinopyroxene trace element patterns. Clinopyroxenes in Group-1b lherzolite NH1408 and Group-2b lherzolite GN1402 show larger variability in trace element patterns compared to the other SB xenoliths. It is accounted for both intra- and intergrain variability (Fig. S5, S8 and S9), despite the lack of major element zonation. In both xenoliths, the REY patterns vary from LREE depleted patterns (like in Group-1a and Group-2a) to LREE enriched, starting from Sm (Fig. S5A and D). With increasing LREE the concentration of U, Th, Pb and Sr are also increasing (Fig. S5C and F). In Group-1b lherzolite NH1408, the incompatible trace element enrichment consistently increases towards one side of the xenolith from the other, although no change in mineral modes or textures can be observed (Fig. S6). In Group-2b lherzolite GN1402 (Fig. S7 and S8) clear connection between the textural position of the clinopyroxenes and their REY patterns was not observed.

In the Group-2b sheared lherzolite RGB1456 (Fig. S9), clinopyroxenes show patterns similar to Group-1a and Group-2a in the cores, and similar to Group-3 compositions (see below) close to spongy rims and cracks (Fig. S1). Additionally, clinopyroxenes in the sheared zone have LREE (from La to Gd), LIL elements and Nb—Ta enrichments and slightly lower Hf—Zr anomaly compared to the Group-3 phlogopite-bearing xenoliths (Fig. 8G and H).

In the Group-2b lherzolite FKG1402 (Fig. S10), two types of REY patterns were observed: a flat one, which plots close to Group-1a and Group-2a clinopyroxenes with $(La/Lu)_N < 1$, and an enriched one in REE from La to Ho, consistent with other flat patterns from Group-2b xenoliths. The LREE enriched clinopyroxene grains are in contact with amphibole overgrowths and amphiboles in orthopyroxene-rich band (Fig. S10B), the LREE depleted clinopyroxene appears further from band (Fig. S10A). Besides REE, the clinopyroxenes in contact with amphiboles are also enriched in Ba, Pb, Sr, Hf and Zr compared to the LREE depleted ones.

5.3.2. Orthopyroxene

The chondrite normalized REY patterns of orthopyroxenes show homogeneous distribution, increasing concentration from La to Lu irrespectively of the group (Fig. S13A and C; Table S9). The orthopyroxenes show positive U, Ta, Pb, Hf and Ti anomalies, close to the PM composition in Group-1 and Group-2 xenoliths (Fig. S13B and D). In Group-3 xenoliths, the orthopyroxene shows the most enriched patterns in LREE (Fig. S13E) and LILE (Fig. S13F). Orthopyroxenes in the equigranular xenolith GS0611 show the most depleted and scattered REY patterns (Fig. S13G). However, similarly to its clinopyroxene (Fig. S13H), a significant positive Pb-anomaly is present in the orthopyroxene of this fine grained xenolith (Fig. S13H).

5.3.3. Amphibole

The chondrite normalized REY patterns of the studied amphiboles are similar to their corresponding clinopyroxenes (Figs. 8 and 9; Table S10). Amphiboles in Group-1a and Group-2a xenoliths have LREE depleted patterns from La to Eu, with $(La/Lu)_N < 1$ (Fig. 9A). The multielement diagram shows a positive Sr and Ti anomaly, and widely scattered LILE and HFSE contents (Fig. 9B). Amphiboles in Group-1a lherzolite SBF1401 have the highest Pb concentrations and show elevated U, Th and Ba abundances, besides the Group-1a lherzolite BEI1404.

In Group-1b and Group-2b xenoliths amphiboles also mimic the trace element patterns of clinopyroxenes: they are enriched in REE ($(La/Lu)_N < 1$) from La to Gd (Fig. 9C). Amphiboles in this groups display lower Ti/Nb and Zr/Nb ratios compared to those in the xenoliths of Group-1a and -2a. Positive Nb and Ta anomaly can be observed in the amphiboles of all the Group-2b xenoliths (Fig. 9D), in amphibole-rich Group-1b xenoliths BEI1401 and TOB1403, and in xenoliths of Group-3b (Table S10).

Amphiboles in Group-3 xenoliths have the most enriched REY patterns of all the studied xenoliths (Fig. 9E). Group-3a amphiboles show enrichment from La to Ho, whereas in Group-3b xenoliths the patterns are convex upward from La to Ho. A negative Ti anomaly ($1 > Ti_N/Ti^*$, where $Ti^* = (Gd_N{}^*Dy_N)^{1/2}$) can be observed in Group-3a xenolith, whereas amphiboles in Group-3b have positive Ti anomalies ($1 < Ti_N/Ti^*$; Fig. 9E). Amphibole of Group-3a harzburgite GN1407 shows much lower Ti, Nb, Ta, Zr, Hf, but slightly higher U, Th and Cr contents than the other xenoliths from Group-3. The Fe-rich amphiboles of the Group-3b xenoliths show the lowest negative U, Th and Pb anomalies. The Nb and Ta content of amphiboles of Group-3 show a positive correlation with Ti-anomaly (Ti^*/Ti_N). The Nb/Ta ratio in Group-3a harzburgite GN1407 is much higher (~121) than those in the other Group-3 xenoliths.

5.3.4. Mica

Phlogopites of Group-3 xenoliths (Table S11) show both intra- and intergrain variability, scattered REY patterns due to low concentrations (<CI chondrite) (Fig. S14A). In all Group-3 xenoliths, except in GN1407 harzburgite, the phlogopites exhibit high positive Ba and Ti anomaly (Fig. S14B). Phlogopites in Group-3b xenoliths are more enriched in Ti than in Group-3a xenoliths. Phlogopites have high amount of Cs and Rb (> 300 × PM), Nb and Ta (>30 × PM) and a positive Sr and Pb anomaly, except in harzburgite GN1407 (Fig. S14B). Nb/Ta is between 15 and 30, except in harzburgite GN1407 where this value is higher (177 in average). Apart from REY and Th, in GN1407 harzburgite phlogopite has the lowest trace element content overall.

6. Equilibrium temperatures and depth of origin

Previously published (Aradi et al., 2017) equilibrium temperatures of the studied SB xenoliths were calculated with three major element thermometers: two-pyroxene thermometer by Brey and Köhler, 1990, T_{BK} Ca-in orthopyroxene thermometer by Brey and Köhler (1990; modified by Nimis & Grütter, 2010, T_{NG}) and Cr-Al in orthopyroxene thermometer by Witt-Eickschen and Seck, 1991, T_{WES} (Table 1). All major element based thermometers provide consistent and robust results in a good agreement (860 and 1093 °C ± 16 °C for T_{BK}; T_{NG}: 894–1056 ± 25 °C; T_{WES}: 897–1053 ± 15 °C, respectively; Aradi et al., 2017),

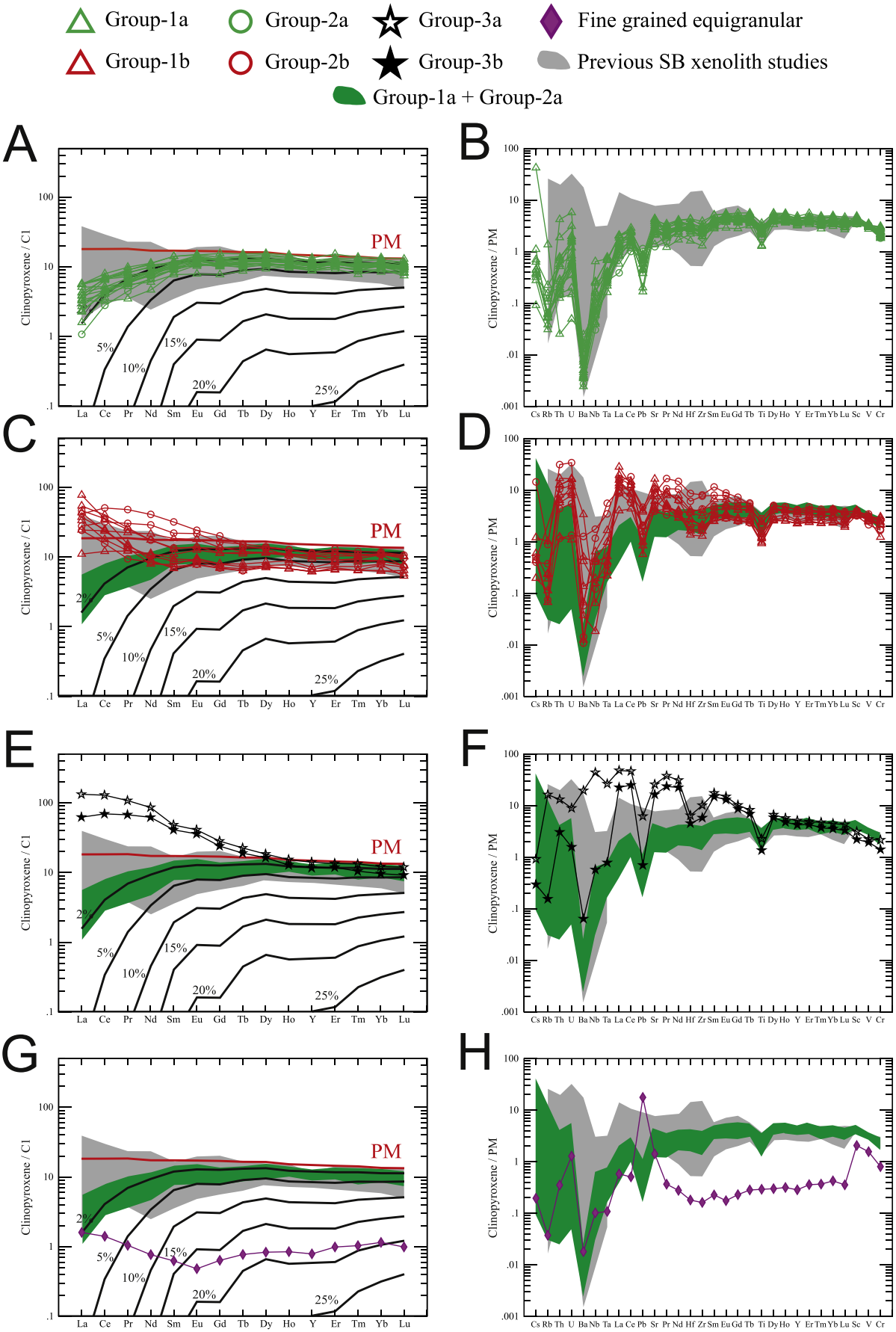

Fig. 8. Rare earth elements + Y (REY), and multielement diagrams of clinopyroxenes in Styrian Basin xenoliths. The REY plots (A, C, E and G) are normalized to the CI, the multielement plots (B, D, F and H) are normalized to the primitive mantle (PM) of McDonough and Sun (1995). REY data are compared to melting curves calculated for anhydrous non-modal fractional melting of clinopyroxene of the primitive mantle (PM, McDonough and Sun, 1995) in the spinel lherzolite facies (Niu, 1997 at 1.5 GPa). References of previous Styrian Basin xenolith studies are from Dobosi et al. (1999) and Coltorti et al. (2007).

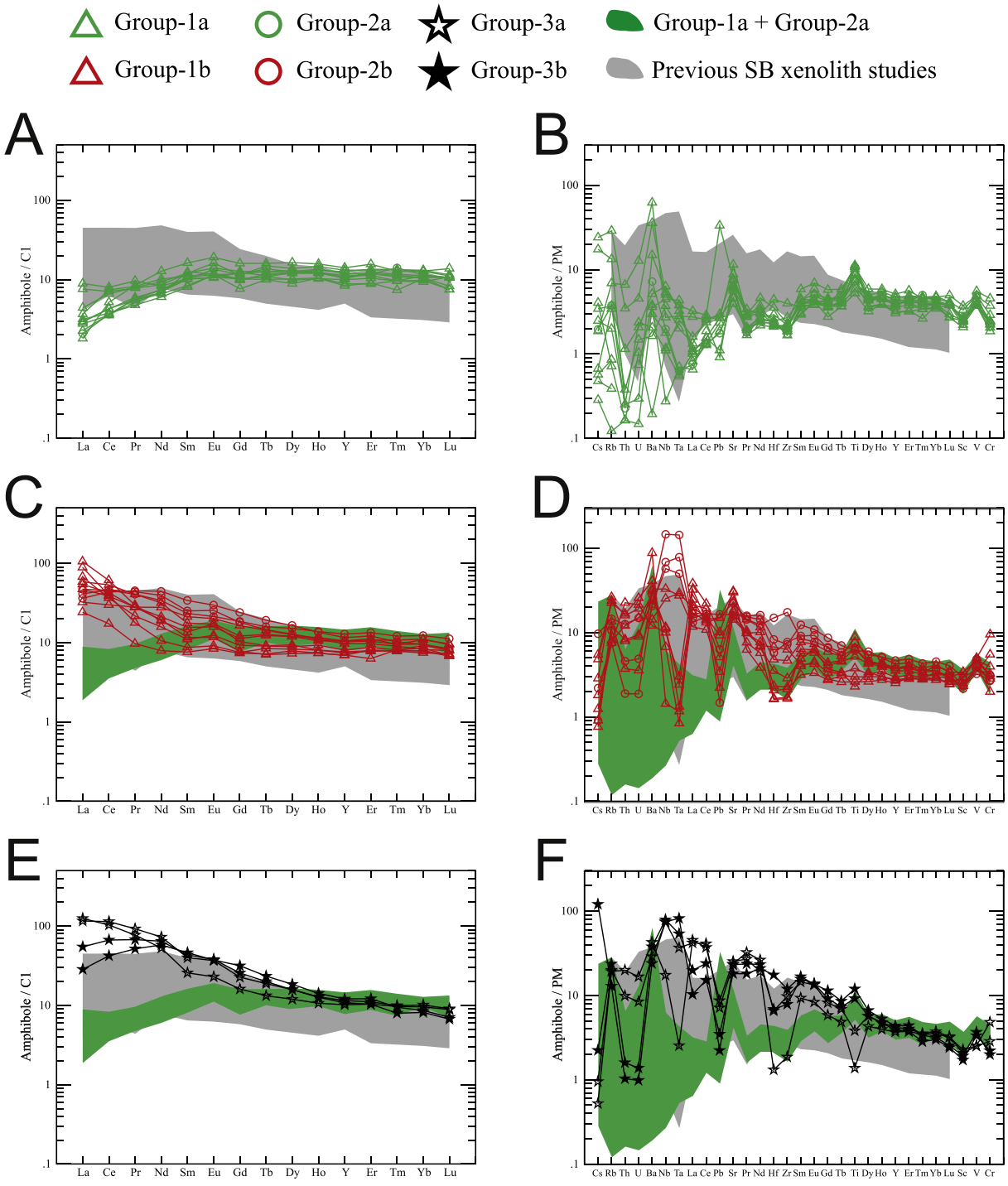

Fig. 9. Rare earth elements + Y (REY), and multielement diagrams of amphiboles in Styrian Basin xenoliths. The REY plots (A, C and E) are normalized to the CI, the multi-element plots (B, D and F) are normalized to the primitive mantle (PM) of McDonough and Sun (1995). References of previous SB xenolith studies are from Coltorti et al. (2007).

except for xenoliths in Group-3 and the fine grained lherzolite GS0611. For these xenoliths, the T_{WES} shows significantly lower equilibrium temperatures (< 825 °C) than T_{BK} and T_{NG}.

Additionally, we used the two-pyroxene, REE thermometer of Liang et al. (2013), which gave slightly higher T range between 915 and 1186 °C. In most of the calculations of T_{REE}, we excluded LREE due to the low concentration and the high uncertainty in orthopyroxene (Fig. S13, Table S9).

The thermal history of the SCLM can be inferred based on the variation in temperatures between the REE and major element based two-pyroxene thermometers (Wang et al., 2015; Yao and Liang, 2015) since the closure temperature of REEs is higher than that of Ca, Mg or Fe in pyroxenes (Liang et al., 2013; Wang et al., 2015). When T_{REE} is higher than T_{BK}, a recent cooling event is expected in the SCLM; in contrast if T_{BK} is higher than T_{REE} a heating event could be assumed (Wang et al., 2015). If the difference between temperatures calculated with the

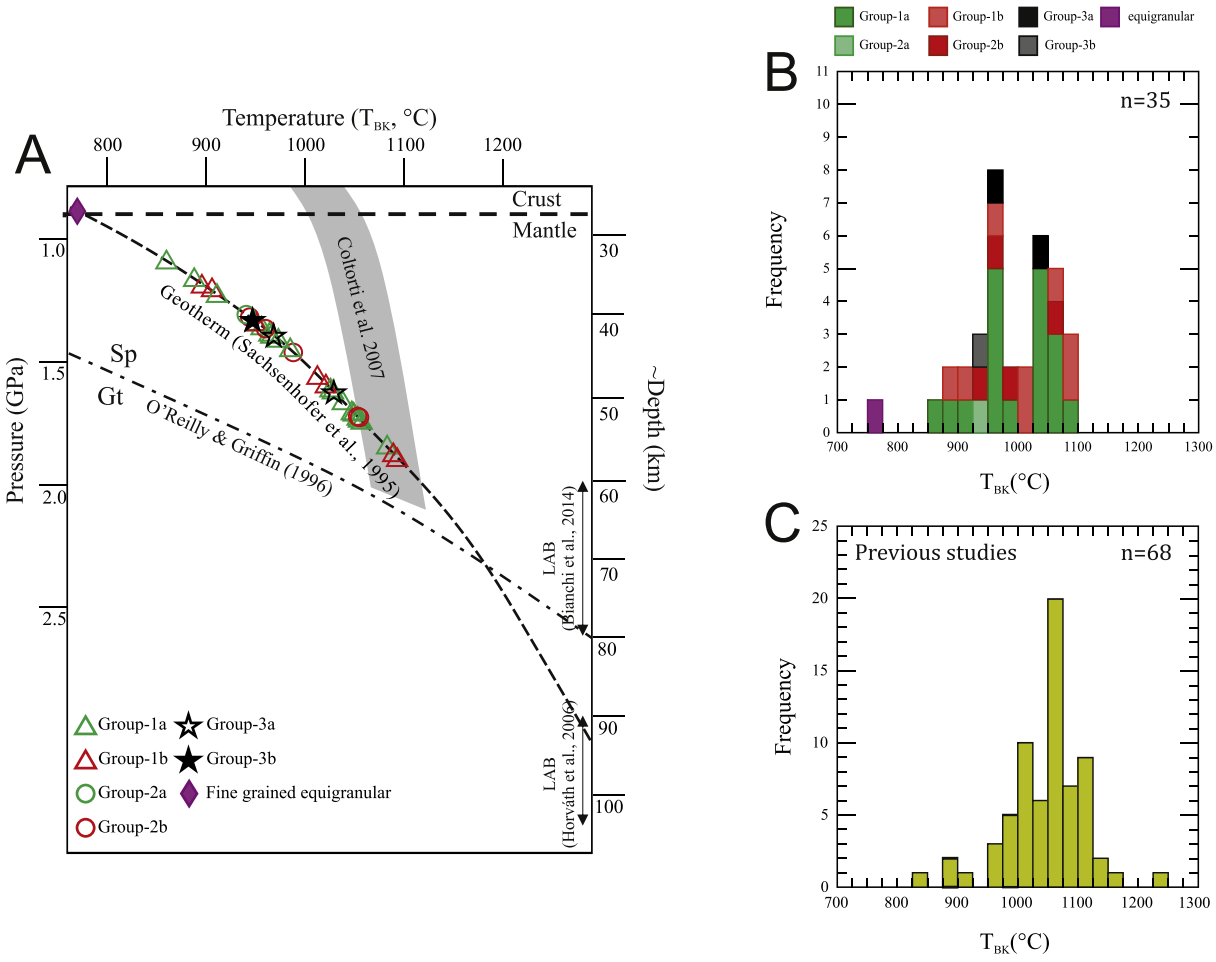

Fig. 10. A: Equilibrium temperatures (T_{BK}) projected onto the recent local geotherm of the Styrian Basin. Spinel (Sp) – Garnet (Gt) phase transformation (dotted-dashed line) is from O'Reilly and Griffin (1996). Crust-mantle boundary (MOHO) depth is based on Horváth et al. (2006). B: Histogram of T_{BK} equilibrium temperatures (Brey and Köhler, 1990) of the studied Styrian Basin xenoliths. The data is compared to the T_{BK} equilibrium temperatures of previously studied Styrian Basin xenoliths based on Kurat et al. (1980, 1991), Vaselli et al. (1996), Dobosi et al. (1999), Falus et al. (2000) and Coltorti et al. (2007).

method of Brey and Köhler (1990) (T_{BK}) and Liang et al. (2013) (T_{REE}) is less than 50 °C, the peridotite is considered well-equilibrated due to its long residence in the lithospheric mantle (Wang et al., 2015).

Half of the xenolith suite shows temperature differences lesser than 50 °C (Fig. S15C); therefore, we can assume that after the last metasomatic event these mantle domains were well equilibrated. However, the other half of the xenolith suite represents mantle domains that show slight temperature variations. Some of the Group-1 and a few of Group-2 xenoliths record slight cooling after the last event, and three xenoliths a slight heating. T_{REE} was ignored in the fine grained equigranular lherzolite GS0611 due to the extremely low REE concentrations in both pyroxenes.

The equilibration pressure of xenoliths was estimated combining the T_{BK} and the local geotherm of the Styrian Basin (Fig. 10) beacuse there are no reliable, major-element geobarometers for spinel-facies peridotites. Based on petrographic observations, the calculated equilibrium temperatures, and the local geotherm, the studied xenoliths were equilibrated in the spinel facies and derived from a ~ 30 km thick domain; approximately from a 30 to 60 km depth range (Fig. 10; Aradi et al., 2017). The depth of the Lithosphere-Asthenosphere Boundary (LAB) is 60–80 km beneath the Styrian Basin (Bianchi et al., 2014). Thus, the studied xenoliths derive from the subcontinental lithospheric mantle. The fine grained equigranular GS0611 xenolith, which records the lowest T_{BK} (770 °C), represents probably the uppermost part of the SCLM (~ 27 km, Horváth et al., 2006) close to the MOHO (Aradi et al., 2017). Compared to previous studies (e.g. Kurat et al., 1991; Vaselli et al., 1996), which mainly focused on the xenoliths of Kapfenstein and Tobaj, xenoliths in our study represent samples from the SCLM from c. 100 °C lower temperature range (Fig. 10), indicating that xenoliths found in previously studied localities may not represent the whole lithospheric column beneath the Styrian Basin.

7. Discussion

7.1. Partial melting in the Styrian Basin SCLM

In order to quantify the degree of the partial melting within the SB upper mantle, we used the REY contents of clinopyroxenes and the Cr# of spinels. For the REY based modeling, we used the anhydrous non-modal fractional model of Niu (1997) using the clinopyroxene composition of the primitive mantle of McDonough and Sun (1995). For the use Cr# of spinels as a melting indicator (Table 1), we followed the model of Hellebrand et al. (2001). Clinopyroxene compositions of most Group-1a and Group-2a xenoliths are close to primitive mantle clinopyroxenes and the maximum degree of partial melting is c. 5% (Fig. 8A). The HREE content of clinopyroxene in Group-1b and Group-2b peridotites can be account by less than 10% fractional melting (Fig. 8C), whereas that of Group-3 xenoliths only records 5% melting (Fig. 8E). In contrast, the low temperature, fine grained equigranular GS0611 lherzolite underwent as much as 20% of melting from a

primitive mantle source (Fig. 8G). The results of Group-1 and Group-2 xenoliths are broadly in agreement with the estimated melt depletion based on the Cr# of spinel using the Hellebrand et al. (2001) melting model (Fig. 7). However, this model predicts higher depletion degrees than the model of Niu (1997), except for GS0611 lherzolite (8% partial melting). Discrepancy between the two models (and the parameters they are based on) are also found in Group-3 xenoliths and in the RGB1415 lherzolite from Group-1b. As discussed below, it is probably related to the extensive crystallization of amphibole at the expense of spinels (e.g. Fig. 2D) resulting in the modification of the composition of spinels. Regardless of the applied model, Group-1b and Group-2b xenoliths underwent minor amount of melt extraction in the spinel facies, whereas in terms of major elements, Group-1a, Group-2a and Group-3 xenoliths represent a fertile mantle domain with a composition similar to primitive mantle. The majority of the previously studied SB xenoliths (Coltorti et al., 2007; Dietrich and Poultidis, 1985; Dobosi et al., 1999; Falus et al., 2000; Kurat et al., 1980, 1991; Richter, 1971; Vaselli et al., 1996) shows similarities to those of fertile Group-1a and Group-2a xenoliths, recording less than ~7% of partial melting.

Our dataset is large enough (35 xenoliths from 13 localities) to make a region-wide comparison of the fertility and depletion of the SCLM across the CPR. Group-1a and Group-2a xenoliths could be considered as fragments of one of the least depleted SCLM in the CPR. Group-1b, Group-2b and Group-3 xenoliths, however, sampled a more complex, geochemically heterogeneous SCLM, which underwent subsequent metasomatism after the partial melting. In the central part of the CPR (Fig. 1A), with the thinnest lithosphere in the region (~70 km; Horváth et al., 2006), xenolith data suggest a moderately depleted SCLM. Protogranular, geochemically more fertile xenoliths, with an asthenospheric origin (Kovács et al., 2012), have experienced 0–5% melt removal from a primitive mantle source (based on Niu, 1997). In contrast, the common poikilitic and recrystallized xenoliths with mosaic equigranular textures show strong depletion, up to 20% (Bali et al., 2007; Berkesi et al., 2012; Embey-Isztin et al., 2014). In the northern margin of the CPR (Nógrád-Gömör, Liptai et al., 2017), the SCLM is more deformed and underwent significantly higher amount of partial melting (i.e. 7–10% in the most fertile peridotites, up to 25% in the most depleted ones) compared to the Styrian Basin. Xenoliths from the Perşani Mountains (Eastern CPR, Transylvania) show fertile compositions similar to the Styrian Basin xenoliths based on both the Cr# of spinel (Falus et al., 2000, 2008; Vaselli et al., 1995) yielding less than 7% melt removal, and the REE content of clinopyroxenes (Chalot-Prat and Boullier, 1997) suggests less than 5% of melt removal.

7.2. Mantle metasomatism in the Styrian Basin SCLM

7.2.1. Pre-Cenozoic metasomatic events

The Group-2 xenoliths display modal heterogeneity, in the form of pyroxene- or olivine-rich veins and modal layering (Fig. 2C and D). In all Group-2 xenoliths, except the sheared RGB1456 lherzolite (Fig. S1), the major element composition of rock forming minerals is homogeneous suggesting that the pyroxene- or olivine-rich veins and layers (Fig. 2C and D) are in chemical equilibrium with the wall rock, although most of them (Group-2b) were also affected by later metasomatic events.

Pyroxene-rich websteritic veins and bands are common in mantle rocks (e.g. Garrido and Bodinier, 1999). Refertilization of the upper mantle by asthenospheric melts could be the main cause of the generation of secondary clinopyroxene in lherzolites (e.g. Lenoir et al., 2001; Le Roux et al., 2007; Varas-Reus et al., 2016 and reference therein). Websterite can mark melt segregation horizons along lherzolite-harzburgite contacts (e.g. Le Roux et al., 2007; Soustelle et al., 2009) in peridotite massifs, or can be formed during thermal erosion of the SCLM, intermingled with olivine-rich domains (Bodinier et al., 2008; Gervilla and Remaidi, 1993). These melt reactions, coeval with melting, could produce homogeneous major and trace element compositions (e.g. Lenoir et al., 2001). In this scenario the olivine-rich and websterite bands might be the result of relatively young melting event(s) in the mantle. However, their formation in the SB should predate the metasomatic event that precipitated hydrous minerals (see in 7.3.4).

Another explanation for the homogeneous major and trace element distribution of Group-2 xenoliths could be that, after the initial heterogeneous distribution of major and trace elements, the whole mantle assemblage is re-equilibrated, including the observed signs of stealth (O'Reilly and Griffin, 2013) cryptic metasomatism in the SCLM (Dawson, 1984). The equilibration of such geochemical heterogeneities (e.g. in the REE distribution) in the pyroxenes takes at least ~1 Ga under lithospheric conditions (1150 °C and 1.5 GPa; Van Orman et al., 2001). Thus, these features in the Styrian Basin SCLM may be considered as results of ancient (>1 Ga) metasomatic events. Additionally, the Neogene fluid-enhanced recrystallization in the lithospheric mantle beneath the SB (Aradi et al., 2017) could also enhance annealing.

7.2.2. Recent geochemical evolution of the Styrian Basin SCLM

The various enriched trace element patterns (Fig. 8) of clinopyroxenes in the SB xenoliths indicate that after partial melting and subsequent ancient refertilization event(s) (discussed in 7.3.1), the xenoliths of Group-1a, −2a, −1b and -2b and − 3 were enriched by different metasomatic agents. Comparing the Group-1b and -2b and Group-3 xenoliths to Group-1a and -2a xenoliths, the former groups have elevated modes of amphiboles (Table 1, Fig. 6D). In Group-1b and Group-2b xenoliths, clinopyroxenes are depleted in basaltic major elements and HREE, but enriched in LREE, Sm, Th, U,Sr, Hf and Zr following the partial melting event (Fig. 8D). Group-1b and Group-2b xenoliths generally have compositionally homogeneous pyroxenes with the exception of five lherzolite xenoliths from Group-1b -2b and -3b (GN1402, NH1408, RGB1456, FKG1402 and TOB1405; Fig. S5–S12). This chemical homogeneity suggests signs of slow metasomatic front propagation (e.g. Bodinier et al., 1990; Le Roux et al., 2007).

There is clear evidence of chromatographic fractionation in three lherzolites NH1408, GN1402 and RGB1456, showing trace-element inhomogeneity in clinopyroxenes on grain scale. In NH1408 and GN1402 xenoliths, besides LREE (from La to Nd, Fig. S5), U, Th, Pb and Sr also show milli- to centimeter-scale heterogeneity in clinopyroxene (Figs. S6 and S9). All these trace elements positively correlate with each other implying contemporaneous enrichment (Fig. S5C). Such trace element fractionation in lithospheric mantle can be driven by infiltration of fluid or melt (O'Reilly and Griffin, 2013 and references therein). The increasing $(La/Yb)_N$ ratio can be a product of an evolved silicate melt, which percolated through this chromatographic column (e.g. Bedini et al., 1997). We assume that the slight and irregular enrichment in U and Th in some of the clinopyroxenes in the Group-1a and Group-2a xenoliths can also be explained by chromatographic process beside the precipitation of amphiboles from a hydrous melt (discussed below).

7.2.3. Formation of the fine grained lherzolite

The fine grained equigranular lherzolite GS0611 is characterized by specific petrographic, crystallographic (Aradi et al., 2017) and geochemical features among the Styrian Basin xenoliths. Based on the extremely low equilibrium temperature ($T_{BK} = 770$ °C), it should represent the uppermost part of the SCLM near the MOHO (Aradi et al., 2017). Texturally similar xenoliths were observed previously in the central part of the CPR (e.g. Bali et al., 2002; Embey-Isztin et al., 2014). Embey-Isztin et al. (2014) classified these rocks as poikilitic xenoliths and the lherzolite GS0611 shows petrographic and geochemical features similar to those xenoliths. Major element composition of clinopyroxenes in lherzolite GS0611 (CaO > 20 wt%; Al_2O_3 < 5 wt%) and spinels (Cr# > 30), U-shaped LREE patterns (Fig. 8G) and significant positive Pb anomaly (Fig. 8H) in the clinopyroxenes are all the characteristic features of the poikilitic xenoliths of Embey-Isztin et al. (2014). However, the equilibrium temperature is much lower compared to those of Embey-Isztin et al. (2014) from the central CPR (ΔT_{BK} ~ 200–250 °C; ΔT_{WES} ~ 50 °C). These poikilitic xenoliths contain elevated Pb contents relative to the dominant lherzolitic xenolith

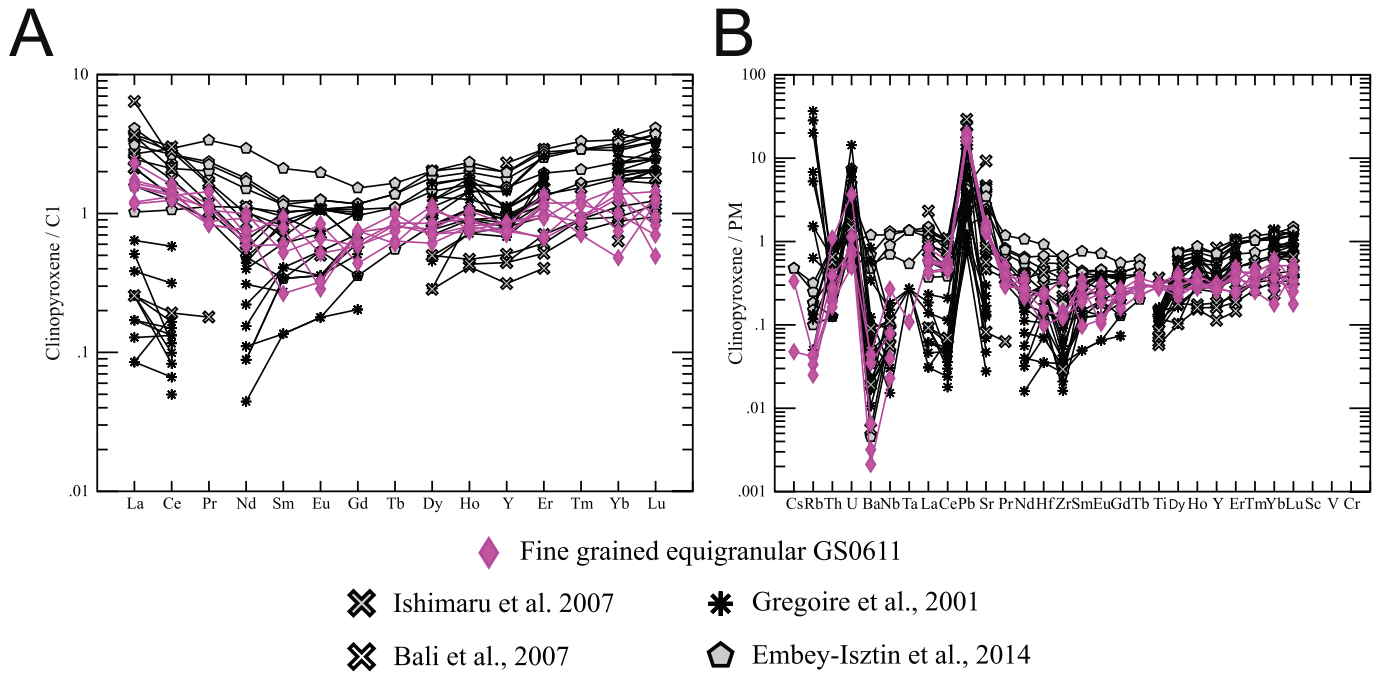

Fig. 11. Comparison of the rare earth element (A) and multielement pattern (B) of clinopyroxene in the GS0611 fine grained equigranular lherzolite with data of similar xenoliths of the Bakony-Balaton Highland (Bali et al., 2007; Embey-Isztin et al., 2014), and with supra-subduction xenoliths from active subduction zones (Grégoire et al., 2001; Ishimaru et al., 2007).

series in the central CPR, which was interpreted as proofs of a strongly eroded lithosphere via percolative fractional crystallization of a carbonatitic melt (Embey-Isztin et al., 2014).

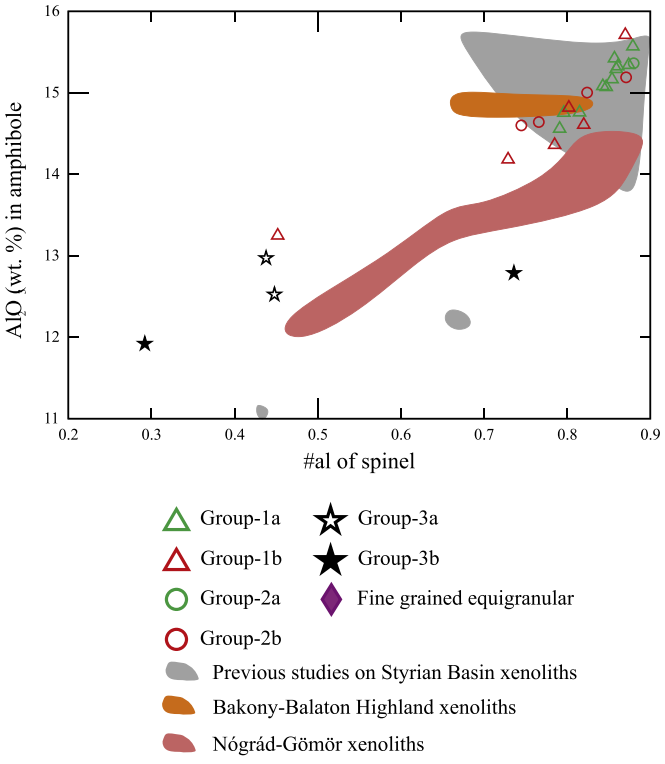

Fig. 12. Variation of Al# ($Al^{3+}/(Cr^{3+}+Al^{3+})$) of spinels vs. Al_2O_3 (wt%) in amphiboles of the Styrian Basin xenoliths. Reference data Styrian Basin xenoliths are taken from Kurat et al. (1991), Dobosi et al. (1999) and Coltorti et al. (2007). Data of the Nógrád-Gömör xenoliths are taken from Liptai et al. (2017), data from the Bakony-Balaton Highland are taken from Hidas et al. (2010).

Note that harzburgites and orthopyroxene-rich xenoliths from sub-arc mantle settings also show similar REY and trace element patterns to GS0611 in both orthopyroxenes and clinopyroxenes (Fig. 11; Kamchatka: Ishimaru et al., 2007; Papua New Guinea: Grégoire et al., 2001). Accordingly, sub-arc mantle xenoliths are derived from a part of the mantle that went through high degree hydrous melting and later metasomatism by fluids released from e.g. a subducted slab into the above lying mantle wedge. The fine grained GS0611 xenolith shows clinopyroxene enrichment along veins (Fig. S3), which formed in a localized shear zone in the presence of melt (Aradi et al., 2017), but these veins are not enriched in orthopyroxene.

In the fine grained equigranular GS0611 xenolith low T_{BK} equilibrium temperature (Table 1), REE (and unrealistic T_{REE}) and Ti contents (Fig. 8G and H) as well as positive Pb and U anomalies in the clinopyroxenes all suggest a fluid-dominated source (e.g. Hermann et al., 2006; Kessel et al., 2005). Since the low REE but high Pb content in clinopyroxene is a specific feature of peridotites of hydrated mantle wedges (Grégoire et al., 2001; Ishimaru et al., 2007), we propose a similar setting for the mantle section represented by GS0611 xenolith. Additionally, the lack of orthopyroxene enrichment could be attributed to separate websterite layers or bands, as explained by boninitic metasomatism in the central CPR (Bali et al., 2007) in a fore-arc setting. However, these lithologies have not been found in the Styrian Basin xenolith suite. Scarcity of the fine grained equigranular xenoliths in the Styrian Basin suggests that this subduction-related metasomatic event was not as extensive as in the central part of the CPR. The fine grained xenolith GS0611 only could have sampled the residual, fluid-enriched metasomatic agents, originating from a subducted slab, which evolved after the crystallization of such orthopyroxene-rich parts in the SCLM.

7.2.4. Formation of amphibole and phlogopite, and the source of the metasomatic agent(s)

REY partition coefficients between coexisting amphiboles and clinopyroxenes in both Group-1 and Group-2 xenoliths are close to the natural (Coltorti et al., 2007; Witt-Eickschen and Harte, 1994) and relevant experimental data (e.g. Adam and Green, 1994), suggesting

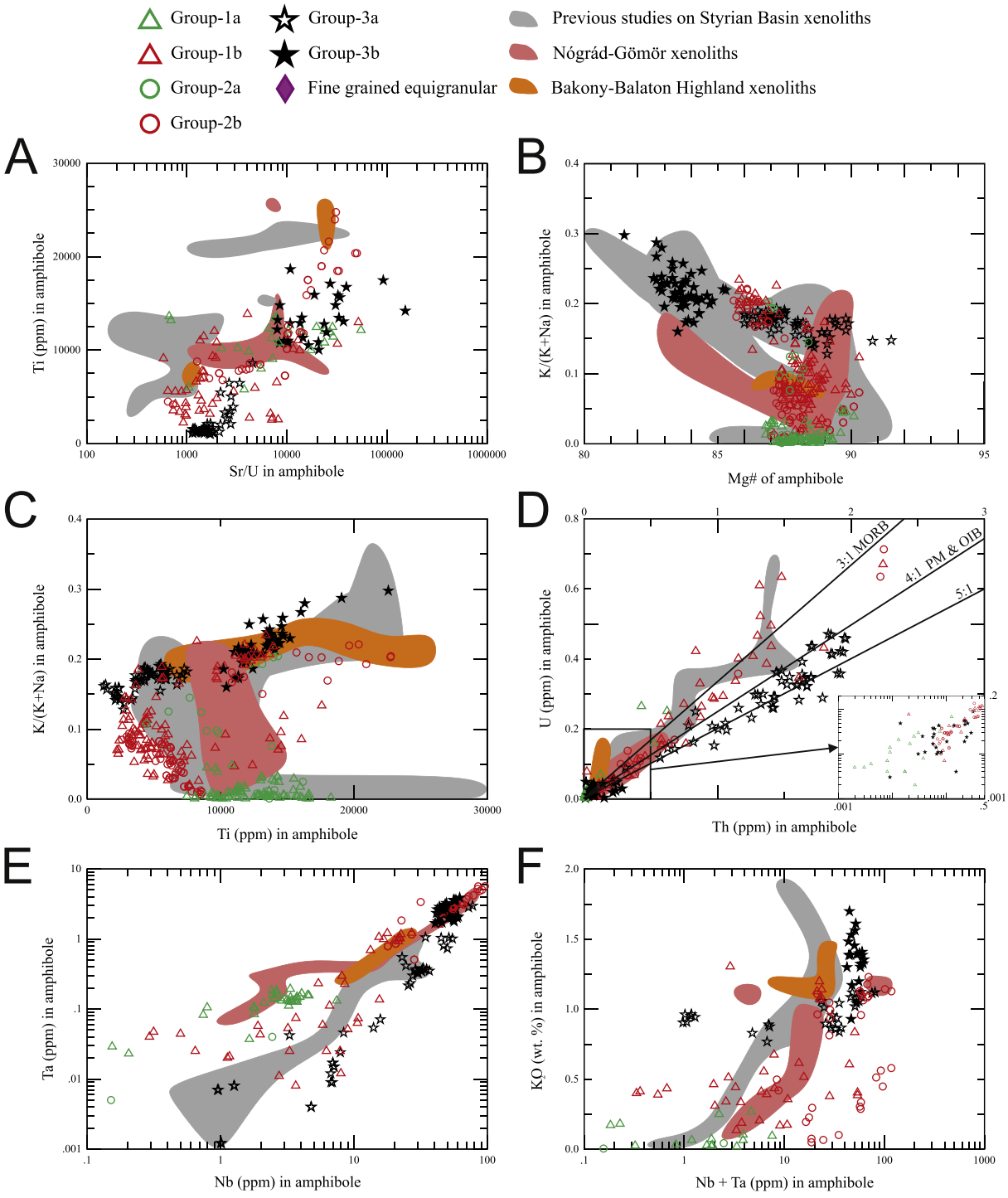

Fig. 13. Scatter plots of the major and trace element geochemistry of amphiboles in the Styrian Basin xenoliths. A: Variation of Sr/U ratio vs. Ti (ppm) in amphiboles. B: Variation of K/(K + Na) ratio vs. Mg# (ΣMg/(ΣMg + ΣFe) of amphiboles. C: Variation of K/(K + Na) ratio vs. Ti (ppm) in amphiboles. D: Variation of U vs. Th (ppm) in amphiboles. The black lines denote the ratio of Th/U (3 and 5, respectively), MORB is the value of average middle ocean ridge basalts (~3); OIB and PM is the value of the average ocean island basalt and the primitive mantle (~4; Sun and McDonough, 1989). E: Variation of Nb vs. Ta (ppm) in amphiboles. F: Variation of Nb + Ta (ppm) vs. K_2O (wt%) in amphiboles. Reference trace element data on Styrian Basin xenoliths are taken from Coltorti et al. (2007), major element data taken from Kurat et al. (1991) and Vaselli et al. (1996). Data of the Nógrád-Gömör xenoliths are taken from Liptai et al. (2017), data from the Bakony-Balaton Highland are taken from Szabó et al. (2009) and Hidas et al. (2010).

equilibrium between them (Fig. S16A and B). Few lherzolites have slightly higher C_{amp}/C_{cpx} ratios for La and for Pr—Eu than expected (Fig. S16A), indicating slight chemical disequilibrium for these elements. The partition coefficients of Th, U, Zr and Hf are close to 1, due to the similar geochemical affinity of these elements in clinopyroxene and amphibole during crystallization. Similar equilibrium between clinopyroxene and amphibole was found in xenoliths from Kapfenstein (Coltorti et al., 2007) and from the Nógrád-Gömör (northern margin of the CPR) (Liptai et al., 2017; Fig. S16). The textural evidence of topotaxial overgrowth of amphiboles on clinopyroxenes (Aradi et al., 2017) suggest that the amphibole formation was the latest recorded metasomatic event in the Styrian Basin xenoliths.

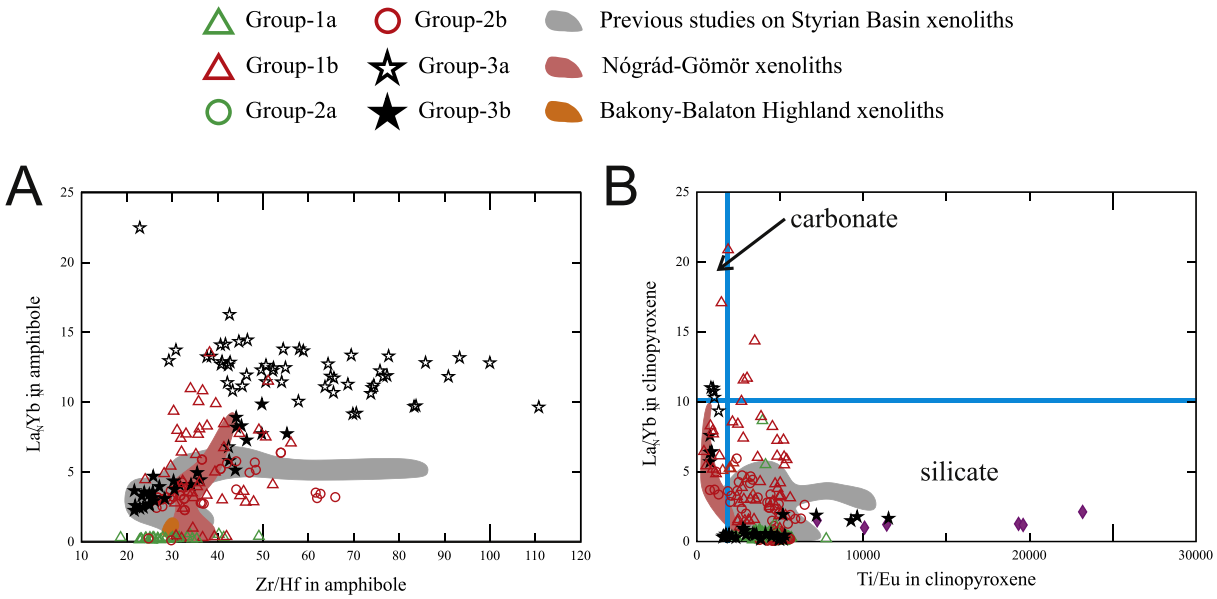

Fig. 14. A: Variation of La_N/Yb_N ratio vs. Zr/Hf ratio in amphiboles of the Styrian Basin xenoliths. B: Variation of Ti/Eu ratio vs. La_N/Yb_N ratio in clinopyroxene. The fields of silicate and carbonate melt metasomatism are from the discrimination diagram of Coltorti et al. (1999). Data from previous studies on Styrian Basin xenoliths are from Dobosi et al. (1999) and Coltorti et al. (2007). Data of the Nógrád-Gömör xenoliths are from Liptai et al. (2017), data from the Bakony-Balaton Highland are from Hidas et al. (2010).

The high Cr# of spinel remnants in Group-1b, Group-2b and Group-3 xenoliths (Fig. 6A) and the strong positive correlation ($R^2 = 0.79$) between the Al_2O_3 and Cr_2O_3 contents of spinels and amphiboles (Fig. 12) suggest that amphiboles grew at the expense of spinels, ortho- and clinopyroxenes under lithospheric mantle conditions. Despite the lack of petrographic evidences, similar observations can be made in Nógrád-Gömör peridotite xenoliths from the Northern Pannonian Basin (Liptai et al., 2017), but not in central Bakony-Balaton Highland Volcanic Field (Szabó et al., 2009; Hidas et al., 2010).

Formation of amphiboles at the expense of spinel and pyroxenes can be the result of the following reaction (Neal, 1988 and references therein):

$$24\ Spinel\ (MgAl_2O_4) + 16\ Diopside\ (CaMgSi_2O_6) + 14\ Enstatite\ (Mg_2Si_2O_6) + Fluid\ (4\ Na_2O + 8\ H_2O) \rightarrow 8\ Pargasite\ (NaCa_2Mg_4Al_3Si_6O_{22}(OH)_2) + 12\ Chromite\ (MgCr_2O_4) + 12\ Olivine\ (Mg_2SiO_4)$$

However, the high REY content of the amphiboles in Group-1b, Group-2b and Group-3 xenoliths (Fig. 9) suggests that alkaline hydrous fluid in itself cannot be the only metasomatic agent since in hydrous fluids the solubility of REY is limited (Kessel et al., 2005 and references therein). The signatures of fluid-originated amphiboles (e.g. low REY content, negative HFSE anomalies, high LILE contents) were not

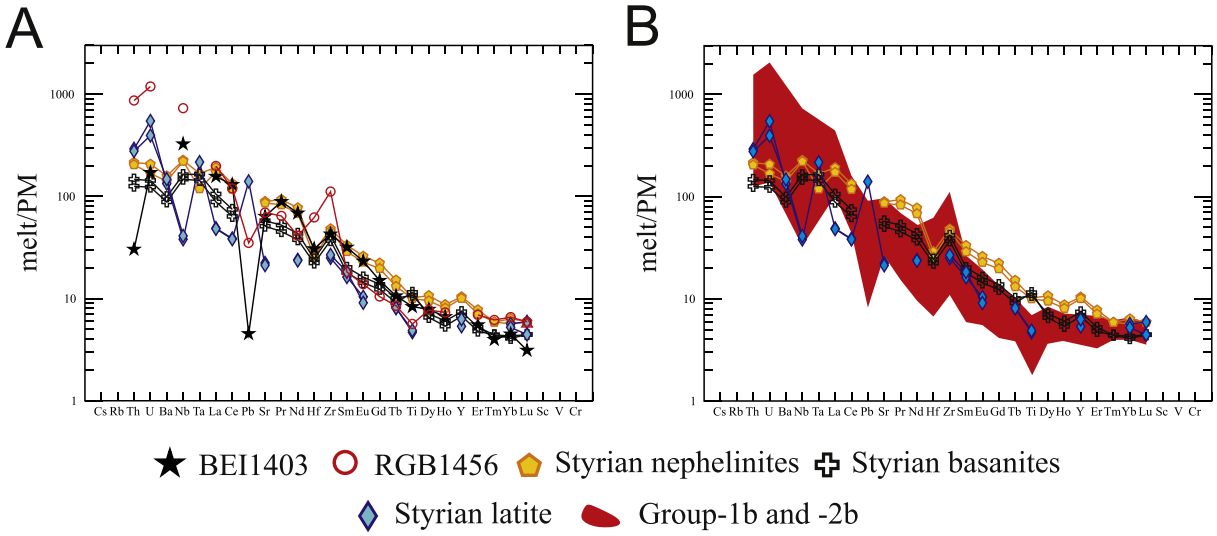

Fig. 15. Multielement (normalized to the primitive mantle, McDonough and Sun, 1995) distribution patterns of the calculated melt compositions in equilibrium with amphiboles of Group-3b wehrlite BEI1403 and Group-2b sheared lherzolite RGB1456 (A); and with the amphiboles of Group-1b and Group-2b xenoliths (B). The calculated melt compositions are compared to that of latite from Gleichenberg (Harangi et al., 1995), basanites (Klöch and Steinberg) and nephelinites (Stradnerkogel and Waltrafelsen) of the Styrian Basin (Ali et al., 2013). The equilibrium melts were calculated with the partition coefficients of Ionov et al. (2002).

observed in the SB xenoliths, thus a volatile-rich melt is the most plausible metasomatic agent in the formation of amphiboles.

Amphiboles and phlogopites in Group-3b xenoliths display at least as high Ti contents (> 2 wt%) as amphiboles in Group-1 xenoliths but much higher Fe contents (FeO > 6 wt%; Table S5, Fig. 8B), the phlogopites are similar to mica megacrysts from Tobaj (Kubovics et al., 1989). These high Ti, K and Fe amphiboles also have elevated Sr/U ratios (Fig. 13A), Nb contents, and less fractionated Nb/Ta and K/(K + Na) ratios (Fig. 13B and C) compared to those in Group-1 and Group-2 xenoliths. All these geochemical properties, i.e. low Mg# (83), high K_2O (~1.3 wt%) and TiO_2 (~ 2.3 wt%) content suggest that amphiboles in Group-3b xenoliths precipitated from a mafic melt in the SCLM, which was suggested also by Coltorti et al. (2007) for amphibole veins in the SB, and by Szabó et al. (2009) in Bakony-Balaton Highland xenoliths (Fig. 13). Moreover, the Ti-poor amphiboles of Group-3a xenoliths could have also precipitated from a mafic melt, which had already precipitated ilmenite or the parental melt had higher volatile (mainly H_2O) content. The early crystallizing Ti-rich phases could remove Ti from the metasomatizing melt and fractionate Nb relative to Ta (e.g. Bodinier et al., 1996; Moine et al., 2001), although ilmenite-bearing xenoliths or Nb- and Ta-bearing microphases (e.g. Bodinier et al., 1996) were not found in SB xenolith suite. In Group-3a xenoliths the high Zr/Hf

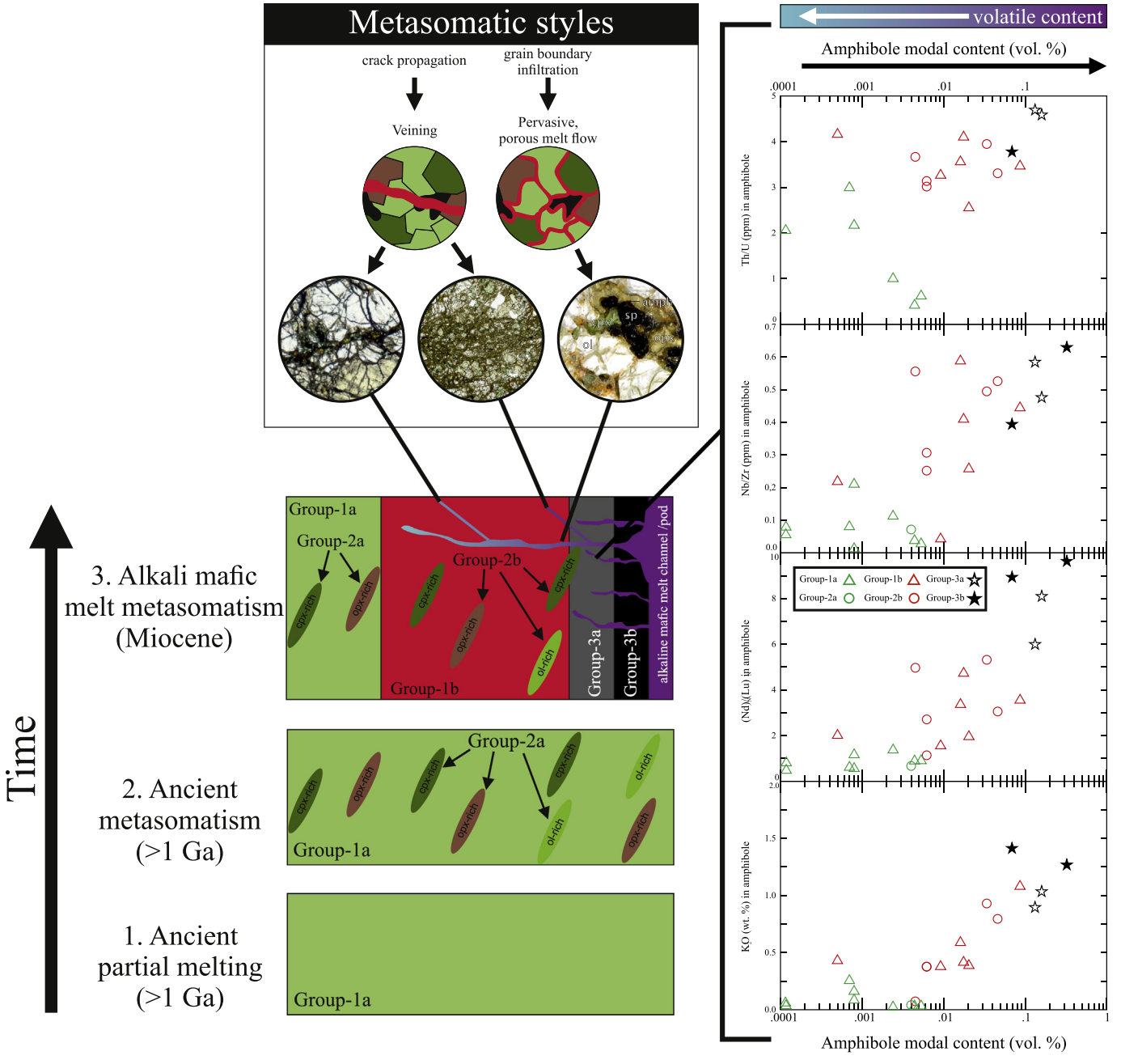

Fig. 16. Flowchart of the geochemical evolution of the Styrian Basin xenoliths. 1. Ancient partial melting event, during which the lithospheric mantle suffered varying amount of melt extraction. 2. Ancient metasomatic events, which resulted in lithological inhomogeneities in the SCLM, represented by the Group-2 xenoliths. 3. Alkali mafic metasomatism, during which the propagating mafic melt fractionated along the lithospheric column, producing Group-1b, −2b and Group-3 mantle segments. On the right side, the most characteristic changes in the amphibole geochemistry is shown upon the fractionation of the alkaline mafic melt as a function of the modal content of amphibole. On the uppermost part of the image the two observed metasomatic styles, melt infiltration along grain boundaries and crack propagation, are presented with a cartoon and with representative petrographic images of the Styrian Basin xenoliths.

(>50) (Fig. 14A) and high Nb/Ta (>500 in harzburgite GN1407) ratios in amphiboles, besides the presence of apatite (Fig. 4F; O'Reilly and Griffin, 2000 and references therein) could be the signs of carbonate melt related metasomatism (e.g. Dupuy et al., 1992). However, on the La_N/Yb_N vs. Ti/Eu discrimination diagram (Coltorti et al., 1999) only xenoliths having heterogeneous clinopyroxenes with highly fractionated LREE/HREE ratios and moderate Ti anomalies plot in the field of carbonate melt metasomatism. Group-1b an -2b xenoliths scatter between the silicate metasomatism field and the carbonate field (Fig. 14B) suggesting mixing of these two sources of melt component (similarly in the case of the Nógrád-Gömör xenolith; Liptai et al., 2017), although carbonate-rich melts can also be evolved products of CO_2-bearing hydrous silicate melts (e.g. Laurora et al., 2001; Zanetti et al., 1999). The apatites in Group-3a xenoliths are rich in Cl (1.9–2.4 wt%) and contain CO_3^{2-} (Fig. S4). The presence of CO_2-rich fluid inclusions in the amphiboles (Aradi et al., 2019) with elevated La_N/Yb_N and Zr/Hf ratios in Group-3a xenoliths also suggests a significant CO_2-bearing component in the H_2O-rich metasomatizing melt.

We calculated the composition of a melt in equilibrium with the amphibole of BEI1403 from Group-3b (highest K_2O content) and the sheared lherzolite RGB1456 based on partition coefficients of Ionov et al., 2002 (Fig. 15A). The Styrian Basin nephelinites, which are assumed to have a source enriched by carbonate melt with the estimated ~5% CO_2 (Ali et al., 2013), display the best fit with the calculated equilibrium melt. Although the Styrian basanites also give a satisfying fit, except in Nb and LREE concentrations (Fig. 15B). The alkaline intermediate rocks (latites) of Gleichenberg (Harangi et al., 1995) can be ruled out as a potential metasomatic agent.

Based on these data, we assume that the parental melt of the metasomatic agents, which formed the amphiboles in Group-3 xenoliths is similar in nature to the nephelinites of the Styrian Basin. Considering that both Group-3a and Group-3b xenoliths show several similar textural (Fig. 5) and geochemical features (Figs. 6 and 9), the source of the metasomatic agent could have been the same for both groups. The evolution of the same source melt is reflected in the difference between the trace element patterns of Group-3a and Group-3b amphiboles (Fig. 9). The lower Ti content in Group-3a amphiboles indicate high H_2O activity (α_{H2O}) in the metasomatic agent (e.g. Zanetti et al., 1996 and references therein). On the U vs. Th plot, which can be indicative of the fluid content in the metasomatizing melt (Keppler, 1996), the amphiboles (Fig. 13D) of Group-3 xenoliths display a distinct array around the Th/U ≈ 5 (similarly to the vein amphiboles of Coltorti et al., 2007). This can be explained by different volatile content of the mafic melt since hydrous melts are more enriched in U compared to Th than H_2O-poor silicate melts (Keppler, 1996). These geochemical differences could have been caused by the suggested propagating peridotite-melt reaction front, in which slightly further from the melt source the crystallization of amphibole could have caused volatile (mainly CO_2 and H_2O) enrichment in the residual melt. Therefore, we suggest that the apatites of Group-3a xenoliths formed from a CO_2- and H_2O-rich silicate melt, which could have been the residuum of the metasomatizing hydrous melt that precipitated amphiboles in Group-3b xenoliths.

Based on the K_2O, Nb and Ta contents (Fig. 13E and F) and Th/U (Fig. 13D) of amphiboles, those in the Group-2b xenoliths could be formed from the same source and at the same time as the Group-3 amphiboles. According to a widely accepted model, these chemical characteristics of amphiboles often generated in melt veins (e.g. Wilshire et al., 1987). Further from the veins (on a xenolith scale), the residual hydrous melt interacts with the peridotite wall rock, crystallizing disseminated hydrous silicates with low Nb and Zr content (Ionov et al., 1997; Moine et al., 2001). The gradually decreasing Nb/Zr ratio of amphiboles from Group-3 towards the Group-1 amphiboles (Fig. 16) suggests that during the percolation of the mafic melt, via open system reactive porous flow, high Nb/Zr amphiboles form with Mg-rich compositions due to the progressive depletion of Ti in the melt (Tiepolo et al., 2001). Additionally, the decreasing Th/U (≈3) in Group-1b and Group-2b amphiboles, like those in previous studies from the CPR (Coltorti et al., 2007; Liptai et al., 2017), also indicate the relative enrichment in H_2O.

The texturally equilibrated pargasite and its enclosed phlogopite flakes (Fig. 4E) reveal a particular mineral assemblage, which is according to our knowledge was not described before in off-cratonic xenoliths in the spinel facies. The rare co-existence and stability of pargasite + phlogopite (in spinel lherzolite, at 1.8 GPa and 950 °C) corresponds to high activity of H_2O and moderate activity of K_2O, since at higher K_2O activities pargasite is replaced by phlogopite (Safonov et al., 2019). Based on the petrographic relationship and crystallization succession of spinel, phlogopite and amphibole (Fig. 4D) in Group-3 xenoliths, we assume that in the initial stage of the mafic melt-wall rock reaction the activity of K_2O and H_2O was sufficient enough to form phlogopite. Consequently, the metasomatic agent, characteristic for Group-1b and -2b xenoliths, could have contained higher amount of H_2O than the metasomatic agent of Group-3, but lower K_2O, thus phlogopite could not crystallize in them. Moreover, melts in equilibrium with Group-1b and -2b amphiboles show more fractioned LREE/HREE patterns (Fig. 15C, Fig. 16) than the nephelinites and basanites of the Styrian Basin, also suggesting precipitation of Group-1b and -2b amphiboles from a more fractionated melt than the Group-3 amphiboles.

In the Group-1a and Group-2a xenoliths the minor amphiboles mimic the trace element distributions (Figs. 8 and 9) of the clinopyroxenes on which they grew (Fig. 2B) topotaxially (Aradi et al., 2017). Enrichment of fluid mobile elements were not observed in these amphiboles (Fig. 9A and B). Previously such metasomatic events were described as caused by "pure H_2O" in the SB (Coltorti et al., 2007; Kurat et al., 1980; Vaselli et al., 1996). We propose that these xenoliths represent the most distant parts of the metasomatized lithospheric column, where the traces of the proposed distant hydrous melt infiltration may be only identified by the nominally anhydrous minerals (Aradi et al., 2017).

8. Geochemical evolution of the SCLM beneath the Styrian Basin

There is no evidence of vertical stratification between the fertile (Group-1a and Group-2a) and the metasomatized (Group-1b and Group-2b) xenoliths based on their equilibrium temperatures. In both xenolith groups, the T_{BK} range between 850 and 1100 °C (Table 1), a lateral geochemical variation can be assumed between the fertile (asthenosphere-like) Group-1a and -2a and the metasomatized (LREE-enriched) Group-1b and -2b xenoliths. These mantle portions with different geochemical properties and histories could have developed within the SCLM laterally, however these fingerprints were erased later due to annealing and chemical re-equilibration at ambient SCLM conditions. The annealing event is pervasive in the SCLM of the SB, and affected all the studied xenoliths, regardless of their geochemical signature. Based on these, we propose that the recent (Neogene) evolution of the lithosphere (i.e. hydrous metasomatism and annealing, Aradi et al., 2017) overwrote the previous state of the SCLM in the vicinity of the xenolith localities. Only the signs of the most recent metasomatism by nephelinitic melts could have been preserved due to this extensive annealing event.

The propagation of melts and fluids in the lithospheric mantle can happen mainly in two ways (O'Reilly and Griffin, 2013): along propagating cracks, and via grain boundary infiltration. The former one can happen with high fluid pressure and instantaneously and the latter one in a continuous network of melt or fluid film during longer time period. In the SB lithospheric mantle, petrography (Figs. 2 and 3) of the modally (in amphiboles) and compositionally (in trace elements) most enriched Group-1b, Group-2b and Group-3 xenoliths suggest that most of the melts migrated along grain boundaries, pervasively metasomatizing the lithospheric section. Instantaneous melt movement

via crack propagation could only be observed in two Group-2b lherzolite xenoliths from Riegersburg (RGB1454, Fig. 2C; and RGB1456, Fig. S1), although in the literature amphibole veins were also described from Kapfenstein (Coltorti et al., 2007; Kurat et al., 1980).

The metasomatic agent as the mafic (nephelinitic) melt should have migrated upwards from the asthenosphere source, forming melt channels (and lenses) in the SCLM (Fig. 16). Close to the channels the agent caused intensive amphibole and phlogopite formation, which metasomatic products contain high amount of basaltic elements (like Ti, Fe), K, LREE and incompatible trace elements as Zr, Hf represented by the Group-3b xenoliths. Further on, the melt became enriched in volatiles (mainly H_2O and CO_2) and fluid-mobile elements (e.g. U and Pb) and depleted in basaltic elements due to the formation of phlogopite and amphibole during the melt-rock reaction. Upon fractionation, the melt became saturated in P and enriched in Cl, leading to apatite crystallization represented by Group-3a xenoliths (Fig. 4F). The residual, volatile-enriched fluids were trapped in the forming amphiboles, confirmed by the presence of CO_2-rich inclusions in the Group-3a harzburgite GN1407, with a significant concentration of Na and SO_4^{2-} (Aradi et al., 2019). Further away from the melt channels (i.e. crystallizing alkaline mafic melt), composition of the metasomatic agent became even more enriched in H_2O and more depleted in basaltic elements and K, LREE and HFSE leading to the formation of smaller amount of amphiboles as observed in the Group-1b and Group-2b xenoliths (Fig. 9). Due to the increasing fluid-pressure, which might cause fracture development in the peridotite, amphiboles also could precipitate in veins and/or veinlets (Fig. 2C). At the furthest parts from the metasomatic channels, the amphiboles in the fertile Group-1a and Group-2a xenoliths do not exhibit enrichment in fluid mobile elements (Fig. 9A and B). This trace element poor hydrous melt metasomatism, which caused no significant geochemical fingerprint, could have affected large part of the lithospheric mantle, irrespectively to their previously generated lithological heterogeneities. The data of structural hydroxyl content of NAMs, CPO and texture data of the Styrian Basin xenoliths (Aradi et al., 2017) are consistent with the conclusion that the wide-spread annealing event caused the elevated structural hydroxyl content in the olivine. The assumption of an external "water" source, which could be a dehydrating subducted slab beneath the Styrian Basin SCLM (Aradi et al., 2017) is supported highly by the geodynamical environment. On the other hand, fluids derived from a subducted slab should have a characteristic geochemical fingerprint (e.g. elevated fluid-mobile element content like Rb, U, Sr, and Pb; fractionated and high Nb/Ta ratio), which were not recognized in the fertile Group-1a and Group-2a xenoliths. We suggest that these elements could have been buffered by the ambient mantle peridotite. Therefore, only a highly diluted fluid with low trace element content and high H_2O activity could have reached the distant ambient mantle rocks, resulting in an elevated structural hydroxyl content of the NAMs. On the other hand, it is worth mentioning, that comparative data of NAMs in ambient mantle rocks from a subduction environment are not available from the literature.

9. Conclusions

Extensive new geochemical dataset on mantle xenoliths from the Styrian Basin allowed to constrain the evolution of the SCLM beneath the region (Fig. 16). Based on the presented major and trace element dataset, the following events were revealed:

- An initial, ancient (might be ≥1 Ga) partial melting event, which slightly affected the fertile Group-1a, Group-2a and Group-3 (<5%), meanwhile Group-2b xenoliths experienced higher amount of melt removal (<10%).
- The fingerprints of old (probably ≥1 Ga to Cenozoic) metasomatic events are present in the Group-2 xenoliths in the form of veins, bands or layers, which caused petrographic heterogeneities (e.g. websterite dunite lithologies), but no geochemical signs of these events were preserved in the minerals.
- The most recent event recorded in the xenoliths is the migration of a hydrous alkaline melt, possibly originating from a nephelinitic melt source. The melt migrated from the asthenosphere and formed melt channels in the SCLM. Closer to the channels (represented by Group-3b) the extensive amount of amphibole and sparse phlogopite crystallized, enriched in basaltic elements (e.g. Ti and Fe), K, LRE and trace elements such as Zr and Hf. Further from the channels, the metasomatic melt got enriched in H_2O, CO_2 and fluid mobile elements (e.g. U, Pb, Cl and P), but the mode of amphiboles decreased (represented by Group-3b,1b and 2b).
- Neogene evolution of the SCLM overwrote the previous state of the upper mantle beneath the Styrian Basin, thus the geochemical signs of the most recent metasomatic event could have been only preserved, which is probably related to the Plio-Pleistocene magmatism in the region.

Declaration of Competing Interest

The authors declare that they have no known competing financial interests or personal relationships that could have appeared to influence the work reported in this paper.

Acknowledgements

We would like to thank the two anonymous reviewers, and the editor Karen Smit for their constructive and valuable comments and suggestions on our manuscript. The initial manuscript was also improved significantly by Vladica Cvetković and Claudio Marchesi, who reviewed the Ph.D. thesis of L. E. Aradi. We would like to thank Bernardo Cesare (University of Padua) for his support for the electron microprobe measurements. Raúl Carampin, Anna Maria Fioretti (University of Padua) and Patrik Konečný (Dionýz Štúr State Geological Institute) are thanked for their help during the electron microprobe measurements. During the field work, Nóra Liptai, Rita Klébesz and Zoltán Kovács provided essential help. This work was completed with the support of the ELTE Institutional Excellence Program (1783-3/2018/FEKUTSRAT) managed by the Hungarian Ministry of Human Capacities to L.E Aradi, L. Patkó and Cs. Szabó. This research was partially funded by the Hungarian Science Foundation (OTKA, 78425 to Cs. Szabó). Károly Hidas and Carlos J. Garrido acknowledge funding from the Ministry of Economy, Industry and Competitiveness (MINECO, Spain) and the State Research Agency (AEI, Spain) with grants no. FPDI-2013-16253 and CGL2016-81085-R, respectively, and from Junta de Andalucia (Spain) research group RNM-131. The study was also supported by a Lendület Research Grant to the CSFK Lendület Pannon Lith$_2$Oscope Research group. This is the 99th publication of the Lithosphere Fluid Research Lab (LRG).

Appendix A. Supplementary data

Supplementary data to this article can be found online at https://doi.org/10.1016/j.lithos.2020.105831.

References

Adam, J., Green, T.H., 1994. The effects of pressure and temperature on the partitioning of Ti, Sr and REE between amphibole, clinopyroxene and basanitic melts. Chem. Geol. 117, 219–233.

Ali, S., Ntaflos, T., Upton, B.G.J., 2013. Petrogenesis and mantle source characteristics of Quaternary alkaline mafic lavas in the western Carpathian–Pannonian Region, Styria, Austria. Chem. Geol. 337–338, 99–113.

Aradi, L.E., Hidas, K., Kovács, I.J., Tommasi, A., Klébesz, R., Garrido, C.J., Szabó, C., 2017. Fluid-enhanced annealing in the subcontinental lithospheric mantle beneath the westernmost margin of the carpathian-pannonian extensional basin system. Tectonics 36, 2987–3011.

Aradi, L.E., Berkesi, M., Szabó, C., 2019. Composition and origin of upper-mantle fluids based on fluid inclusions in amphibole-rich harzburgite xenoliths from the Styrian Basin. Hungarian. 149. Földtani Közlöny, pp. 35–49.

Arai, S., 1987. An estimation of the least depleted spinel peridotite on the basis of olivine-spinel mantle array. Neues Jb. Mineral. Monat. 8, 347–354.
Awonusi, A., Morris, M.D., Tecklenburg, M.M.J., 2007. Carbonate Assignment and Calibration in the Raman Spectrum of Apatite. Calcif. Tissue Int. 81, 46–52.
Bada, G., Horváth, F., 2001. On the structure and tectonic of the Pannonian Basin and surrounding orogens. Acta Geol. Hung. 44, 301–327.
Bali, E., Szabó, C.S., Vaselli, O., Török, K., 2002. Significance of silicate melt pockets in upper mantle xenoliths from the Bakony–Balaton Highland Volcanic Field, Western Hungary. Lithos 61, 79–102.
Bali, E., Falus, G., Szabó, C.S., Peate, D.W., Hidas, K., Torok, K., Ntaflos, T., 2007. Remnants of boninitic melts in the upper mantle beneath the central Pannonian Basin? Mineral. Petrol. 90, 51–72.
Balogh, K., Ebner, F., Ravasz, C., Herrmann, P., Lobitzer, H., Solti, G., 1994. K/Ar-Alter tertiärer Vulkanite der südöstlichen Steiermark und des südlichen Burgenlandes. Jubiläumsschrift 20, 55–72.
Bedini, R.M., Bodinier, J.L., Dautria, J.M., Morten, L., 1997. Evolution of LILE-enriched small melt fractions in the lithospheric mantle: a case study from the East African Rift. Earth Planet. Sci. Lett. 153, 67–83.
Berkesi, M., Guzmics, T., Szabó, C.S., Dubessy, J., Bodnar, R.J., Hidas, K., Ratter, K., 2012. The role of CO2-rich fluids in trace element transport and metasomatism in the lithospheric mantle beneath the Central Pannonian Basin, Hungary, based on fluid inclusions in mantle xenoliths. Earth Planet. Sci. Lett. 331, 8–20.
Bianchi, I., Miller, M.S., Bokelmann, G., 2014. Insights on the upper mantle beneath the Eastern Alps. Earth Planet. Sci. Lett. 403, 199–209.
Bodinier, J.L., Vasseur, G., Vernieres, J., Dupuy, C., Fabries, J., 1990. Mechanisms of mantle metasomatism: geochemical evidence from the lherz orogenic peridotite. J. Petrol. 31, 597–628.
Bodinier, J.I., Merlet, C., Bedini, R.M., Simien, F., Remaidi, M., Garrido, C.J., 1996. Distribution of niobium, tantalum, and other highly incompatible trace elements in the lithospheric mantle: the spinel paradox. Geochim. Cosmochim. Acta 60, 545–550.
Bodinier, J.-L., Garrido, C.J., Chanefo, I., Bruguier, O., Gervilla, F., 2008. Origin of pyroxenite–peridotite veined mantle by refertilization reactions: evidence from the Ronda peridotite (Southern Spain). J. Petrol. 49, 999–1025.
Bojar, H.-P., Bojar, A.-V., Halas, S., Wójtowicz, A., 2013. K/Ar geochronology of igneous amphibole phenocrysts in Miocene to Pliocene volcaniclastics, Styrian Basin, Austria. Geol. Q. 57.
Brey, G.P., Köhler, T., 1990. Geothermobarometry in Four-phase lherzolites II. New thermobarometers, and practical assessment of existing thermobarometers. J. Petrol. 31, 1353–1378.
Chalot-Prat, F., Boullier, A.-M., 1997. Metasomatism in the subcontinental mantle beneath the Eastern Carpathians (Romania): new evidence from trace element geochemistry. Contrib. Mineral. Petrol. 129, 284–307.
Coltorti, M., Bonadiman, C., Hinton, R.W., Siena, F., Upton, B.G.J., 1999. Carbonatite metasomatism of the oceanic upper mantle: evidence from clinopyroxenes and glasses in ultramafic xenoliths of Grande Comore, Indian Ocean. J. Petrol. 40, 133–165.
Coltorti, M., Bonadiman, C., Faccini, B., Ntaflos, T., Siena, F., 2007. Slab melt and intraplate metasomatism in Kapfenstein mantle xenoliths (Styrian Basin, Austria). Lithos 94, 66–89.
Csontos, L., Vörös, A., 2004. Mesozoic plate tectonic reconstruction of the Carpathian region. Palaeogeogr. Palaeoclimatol. Palaeoecol. 210, 1–56.
Dando, B.D.E., Stuart, G.W., Houseman, G.A., Hegedüs, E., Brückl, E., Radovanović, S., 2011. Teleseismic tomography of the mantle in the Carpathian–Pannonian region of Central Europe. Geophys. J. Int. 186, 11–31.
Dawson, J.B., 1984. Contrasting types of upper-mantle metasomatism? In: Kornprobst, J. (Ed.), Developments in Petrology. Elsevier, pp. 289–294
Dietrich, H., Poultidis, H., 1985. Petrology of ultramafic xenoliths in alkali basalts from Kloch and Stradner Kogel (Styria, Austria). Neues Jahrbuch für Mineralogie-Abhandlungen 151, 131–140.
Dobosi, G., Kurat, G., Jenner, G.A., Brandstatter, F., 1999. Cryptic metasomatism in the upper mantle beneath Southeastern Austria: a laser ablation microprobe-ICP-MS study. Mineral. Petrol. 67, 143–161.
Dobosi, G., Jenner, G., Embey-Isztin, A., Downes, H., 2010. Cryptic metasomatism in clino- and orthopyroxene in the upper mantle beneath the Pannonian region. In: Coltorti, M. (Ed.), Petrological Evolution of the European Lithospheric Mantle: From Archaean to Present Day. Geological Society, London.
Downes, H., 1999. Heterogeneity in the lithospheric mantle beneath the European plate: a continent-wide review. Ofioliti 24, 91–92.
Downes, H., Embey-Isztin, A., Thirlwall, M.F., 1992. Petrology and geochemistry of spinel peridotite xenoliths from the western Pannonian Basin (Hungary): evidence for an association between enrichment and texture in the upper mantle. Contrib. Mineral. Petrol. 109, 340–354.
Dupuy, C., Liotard, J.M., Dostal, J., 1992. Zr/hf fractionation in intraplate basaltic rocks: Carbonate metasomatism in the mantle source. Geochim. Cosmochim. Acta 56, 2417–2423.
Ebner, F., Sachsenhofer, R.F., 1995. Palaeogeography, subsidence and thermal history of the Neogene Styrian Basin (Pannonian basin system, Austria). Tectonophysics 242, 133–150.
Embey-Isztin, A., Downes, H., James, D.E., Upton, B.G.J., Dobosi, G., Ingram, G.A., Harmon, R.S., Scharbert, H.G., 1993. The petrogenesis of Pliocene alkaline volcanic rocks from the Pannonian Basin, Eastern Central Europe. J. Petrol. 34, 317–343.
Embey-Isztin, A., Dobosi, G., Altherr, R., Meyer, H.P., 2001. Thermal evolution of the lithosphere beneath the western Pannonian Basin: evidence from deep-seated xenoliths. Tectonophysics 331, 285–306.
Embey-Isztin, A., Dobosi, G., Bodinier, J.-L., Bosch, D., Jenner, G.A., Pourtales, S., Bruguier, O., 2014. Origin and significance of poikilitic and mosaic peridotite xenoliths in the western Pannonian Basin: geochemical and petrological evidences. Contrib. Mineral. Petrol. 168.
Falus, G., Szabó, C.S., Vaselli, O., 2000. Mantle upwelling within the Pannonian Basin: evidence from xenolith lithology and mineral chemistry. Terra Nova 12, 295–302.
Falus, G., Tommasi, A., Ingrin, J., Szabó, C.S., 2008. Deformation and seismic anisotropy of the lithospheric mantle in the southeastern Carpathians inferred from the study of mantle xenoliths. Earth Planet. Sci. Lett. 272, 50–64.
Fodor, L., Csontos, L., Bada, G., Györfi, I., Benkovics, L., 1999. Tertiary tectonic evolution of the Pannonian basin system and neighbouring orogens: a new synthesis of palaeostress data. In: Durand, B., Jolivet, L.F.H., Séranne, M. (Eds.), The Mediterranean Basins: Tertiary Extension within the Alpine Orogen. - Geological Society. Special Publications, London, pp. 295–334.
Garrido, C.J., Bodinier, J.-L., 1999. Diversity of mafic rocks in the ronda peridotite: evidence for pervasive melt–rock reaction during heating of subcontinental lithosphere by upwelling asthenosphere. J. Petrol. 40, 729–754.
Gervilla, F., Remaidi, M., 1993. Field trip to the Ronda ultramafic massif: an example of asthenosphere–lithosphere interaction. Ofioliti 18, 21–35.
Grégoire, M., McInnes, B.I.A., O'Reilly, S.Y., 2001. Hydrous metasomatism of oceanic sub-arc mantle, Lihir, Papua New Guinea: part 2. Trace element characteristics of slab-derived fluids. Lithos 59, 91–108.
Harangi, S., 2001a. Neogene magmatism in the Alpine-Pannonian transition Zone - a model for melt generation in a complex geodynamic setting. Acta Vulcanol. 13, 25–39.
Harangi, S., 2001b. Neogene to quaternary volcanism of the carpathian-pannonian region - a review. Acta Geol. Hung. 44, 223–258.
Harangi, S., Wilson, M., Tonarini, S., 1995. Petrogenesis of Neogene potassic volcanic rocks in the Pannonian Basin. Acta Vulcanol. 7, 125–134.
Harangi, S., Jankovics, M.É., Sági, T., Kiss, B., Lukács, R., Soós, I., 2015. Origin and geodynamic relationships of the late Miocene to Quaternary alkaline basalt volcanism in the Pannonian basin, eastern–Central Europe. Int. J. Earth Sci. 104, 2007–2032.
Hawthorne, F.C., Oberti, R., Harlow, G.E., Maresch, W.V., Martin, R.F., Schumacher, J.C., Welch, M.D., 2012. Nomenclature of the amphibole supergroup. Am. Mineral. 97, 2031–2048.
Hellebrand, E., Snow, J.E., Dick, H.J., Hofmann, A.W., 2001. Coupled major and trace elements as indicators of the extent of melting in mid-ocean-ridge peridotites. Nature 410, 677–681.
Heritsch, F., 1908. Über einige Einschlüsse und vulkanische Bomben von Kapfenstein. Centralblatt für Mineralogie 10, 297–305.
Heritsch, H., 1967. Über die Magmenentfaltung des steirisches Vulkanbogens. Contrib. Mineral. Petrol. 15, 330–344.
Hermann, J., Spandler, C., Hack, A., Korsakov, A.V., 2006. Aqueous fluids and hydrous melts in high-pressure and ultra-high pressure rocks: Implications for element transfer in subduction zones. Lithos 92, 399–417.
Hidas, K., Guzmics, T., Szabó, C.S., Kovacs, I., Bodnar, R.J., Zajacz, Z., Nedli, Z., Vaccari, L., Perucchi, A., 2010. Coexisting silicate melt inclusions and H2O-bearing, CO2-rich fluid inclusions in mantle peridotite xenoliths from the Carpathian-Pannonian region (Central Hungary). Chem. Geol. 274, 1–18.
Hinterlechner-Ravnik, A., Mišič, M., 1986. Peridotite nodules in the basaltic tuff at Grad in Prekmurje (Peridotitne nodule v bazaltnem tufu pri Gradu v Prekmurju). Geologija 28, 205–218.
Horváth, F., Bada, G., Szafián, P., Tari, G., Ádám, A., 2006. Formation and deformation of the Pannonian Basin: Constraints from observational data. In: Gee, D.G., Stephenson, R. (Eds.), European Lithosphere Dynamics. The Geological Society of London, London, pp. 191–206.
Horváth, F., Musitz, B., Balázs, A., Végh, A., Uhrin, A., Nádor, A., Koroknai, B., Pap, N., Tóth, T., Wórum, G., 2015. Evolution of the Pannonian basin and its geothermal resources. Geothermics 53, 328–352.
Huismans, R.S., Podladchikov, Y.Y., Cloetingh, S., 2001. Dynamic modeling of the transition from passive to active rifting, application to the Pannonian basin. Tectonics 20, 1021–1039.
Ionov, D.A., Griffin, W.L., O'Reilly, S.Y., 1997. Volatile-bearing minerals and lithophile trace elements in the upper mantle. Chem. Geol. 141, 153–184.
Ionov, D.A., Bodinier, J.-L., Mukasa, S.B., Zanetti, A., 2002. Mechanisms and sources of mantle metasomatism: major and trace element compositions of peridotite xenoliths from spitsbergen in the context of numerical modelling. J. Petrol. 43, 2219–2259.
Ishimaru, S., Arai, S., Ishida, Y., Shirasaka, M., Okrugin, V.M., 2007. Melting and multi-stage metasomatism in the mantle wedge beneath a frontal arc inferred from highly depleted peridotite xenoliths from the Avacha Volcano, Southern Kamchatka. J. Petrol. 48, 395–433.
Jochum, K.P., Nohl, U., Herwig, K., Lammel, E., Stoll, B., Hofmann, A.W., 2005. GeoReM: a new geochemical database for reference materials and isotopic standards. Geostand. Geoanal. Res. 29, 333–338.
Jugovics, L., 1915. Az Alpok keleti végződése alján és a Vas vármegyei Kis Magyar Alföldön felbukkanó bazaltok és bazalttufák. I. rész. Magyar Állami Földtani Intézet Éves Jelentése 49–73.
Kázmér, M., Kovács, S., 1985. Permian-Palaeogene paleogeography along the eastern part of the Insubric-Periariatic Lineament system: evidence for continental escape of the Bakony-Drauzug Unit. Acta Geol. Hung. 28, 71–84.
Keppler, H., 1996. Constraints from partitioning experiments on the composition of subduction-zone fluids. Nature 380, 237–240.
Kessel, R., Schmidt, M.W., Ulmer, P., Pettke, T., 2005. Trace element signature of subduction-zone fluids, melts and supercritical liquids at 120–180 km depth. Nature 437, 724.
Kovács, I., Falus, G., Stuart, G., Hidas, K., Szabó, C.S., Flower, M.J., Hegedűs, E., Posgay, K., Zilahi-Sebess, L., 2012. Seismic anisotropy and deformation patterns in upper mantle

xenoliths from the central Carpathian–Pannonian region: Asthenospheric flow as a driving force for Cenozoic extension and extrusion? Tectonophysics 514–517.
Kubovics, I., Szabó, C.S., Solymos, K., 1989. Geochemistry of phlogopites in ultramafic xenoliths of lamprophyre dykes (Alcsutdoboz, Hungary). Neues Jb. Mineral. Abh. 161, 171–191.
Kurat, G., Palme, H., Spettel, B., Baddenhausen, H., Hofmeister, H., Palme, C., Wanke, H., 1980. Geochemistry of Ultramafic Xenoliths from Kapfenstein, Austria - evidence for a variety of upper mantle processes. Geochim. Cosmochim. Acta 44, 45–60.
Kurat, G., Embeyisztin, A., Kracher, A., Scharbert, H.G., 1991. The upper mantle beneath kapfenstein and the transdanubian volcanic region, E Austria and W Hungary - a Comparison. Mineral. Petrol. 44, 21–38.
Laurora, A., Mazzucchelli, M., Rivalenti, G., Vannucci, R., Zanetti, A., Barbieri, M.A., Cingolani, C.A., 2001. Metasomatism and melting in carbonated peridotite xenoliths from the mantle wedge: the gobernador gregores case (Southern Patagonia). J. Petrol. 42, 69–87.
Le Roux, V., Bodinier, J.L., Tommasi, A., Alard, O., Dautria, J.M., Vauchez, A., Riches, A.J.V., 2007. The Lherz spinel lherzolite: Refertilized rather than pristine mantle. Earth Planet. Sci. Lett. 259, 599–612.
Lenoir, X., Garrido, C.J., Bodinier, J.-L., Dautria, J.-M., Gervilla, F., 2001. The recrystallization front of the ronda peridotite: evidence for melting and thermal erosion of subcontinental lithospheric mantle beneath the Alboran Basin. J. Petrol. 42, 141–158.
Liang, Y., Sun, C., Yao, L., 2013. A REE-in-two-pyroxene thermometer for mafic and ultramafic rocks. Geochim. Cosmochim. Acta 102, 246–260.
Liptai, N., Patkó, L., Kovács, I.J., Hidas, K., Pintér, Z., Jeffries, T., Zajacz, Z., O'Reilly, S.Y., Griffin, W.L., Pearson, N.J., Szabó, C.S., 2017. Multiple Metasomatism beneath the Nógrád–Gömör Volcanic Field (Northern Pannonian Basin) Revealed by Upper Mantle Peridotite Xenoliths. J. Petrol. 58, 1107–1144.
McDonough, W.F., Sun, S.-S., 1995. The composition of the Earth. Chem. Geol. 120, 223–253.
Miller, C., Zanetti, A., Thöni, M., Konzett, J., Klötzli, U., 2012. Mafic and silica-rich glasses in mantle xenoliths from Wau-en-Namus, Libya: Textural and geochemical evidence for peridotite–melt reactions. Lithos 128–131, 11–26.
Mitterbauer, U., Behm, M., Brückl, E., Lippitsch, R., Guterch, A., Keller, G.R., Koslovskaya, E., Rumpfhuber, E.-M., Šumanovac, F., 2011. Shape and origin of the East-Alpine slab constrained by the ALPASS teleseismic model. Tectonophysics 510, 195–206.
Moine, B.N., Grégoire, M., O'Reilly, S.Y., Sheppard, S.M.F., Cottin, J.Y., 2001. High field strength element fractionation in the upper mantle: evidence from amphibole-rich composite mantle xenoliths from the Kerguelen Islands (Indian Ocean). J. Petrol. 42, 2145–2167.
Neal, C.R., 1988. The origin and composition of metasomatic fluids and amphiboles beneath Malaita, Solomon Islands. J. Petrol. 29, 149–179.
Nimis, P., Grütter, H., 2010. Internally consistent geothermometers for garnet peridotites and pyroxenites. Contrib. Mineral. Petrol. 159, 411–427.
Niu, Y., 1997. Mantle melting and melt extraction processes beneath ocean ridges: evidence from abyssal peridotites. J. Petrol. 38, 1047–1074.
O'Reilly, S., Griffin, W., 1996. 4-D lithosphere mapping: methodology and examples. Tectonophysics 262, 3–18.
O'Reilly, S.Y., Griffin, W.L., 2000. Apatite in the mantle: implications for metasomatic processes and high heat production in Phanerozoic mantle. Lithos 53, 217–232.
O'Reilly, S.Y., Griffin, W.L., 2013. Mantle Metasomatism, Metasomatism and the Chemical Transformation of Rock: The Role of Fluids in Terrestrial and Extraterrestrial Processes. Springer, Berlin Heidelberg, Berlin, Heidelberg, pp. 471–533.
Paton, C., Hellstrom, J., Paul, B., Woodhead, J., Hergt, J., 2011. Iolite: Freeware for the visualisation and processing of mass spectrometric data. J. Anal. At. Spectrom. 26, 2508–2518.
Pearce, N.J.G., Perkins, W.T., Westgate, J.A., Gorton, M.P., Jackson, S.E., Neal, C.R., Chenery, S.P., 1997. A compilation of new and published major and trace element data for NIST SRM 610 and NIST SRM 612 glass reference materials. Geostand. Newslett. 21, 115–144.
Pécskay, Z., Lexa, J., Szakács, A., Seghedi, I., Balogh, K., Konečny, V., Zelenka, T., Kovac, M., Póka, T., Fülöp, A., Márton, E., Panaiotu, C., Cvetkovič, V., 2006. Geochronology of neogene magmatism in the Carpathian arc and intra-Carpathian area. Geol. Carpath. 57, 511–530.
Pouchou, J.-L., Pichoir, F., 1991. Quantitative analysis of homogeneous or stratified microvolumes applying the model "PAP". In: Heinrich, K.F.J., Newbury, D.E. (Eds.), Electron Probe Quantitation. Springer US, Boston, MA, pp. 31–75.
Qorbani, E., Bianchi, I., Bokelmann, G., 2015. Slab detachment under the Eastern Alps seen by seismic anisotropy. Earth Planet. Sci. Lett. 409, 96–108.
Ratschbacher, L., Frisch, W., Linzer, H.-G., Marle, O., 1991. Lateral extrusion in the Eastern Alps, part 2: Structural analysis. Tectonics 10, 257–271.
Richter, W., 1971. Ariégite, spinell-peridotite und phlogopit-klinopyroxenite aus dem Tuff von Tobaj im Südlichen Burgenland. Mineral. Petrol. 16, 227–251.
Safonov, O., Butvina, V., Limanov, E., 2019. Phlogopite-Forming Reactions as Indicators of Metasomatism in the Lithospheric Mantle. Minerals 9, 685. https://doi.org/10.3390/min9110685.
Soustelle, V., Tommasi, A., Bodinier, J.L., Garrido, C.J., Vauchez, A., 2009. Deformation and reactive melt transport in the mantle lithosphere above a large-scale partial melting domain: the Ronda Peridotite Massif, Southern Spain. J. Petrol. 50, 1235–1266.
Streckeisen, A., 1976. To each plutonic rock its proper name. Earth Sci. Rev. 12, 1–33.
Sun, S.-S., McDonough, W.-S., 1989. Chemical and isotopic systematics of oceanic basalts: implications for mantle composition and processes. Geol. Soc. Lond., Spec. Publ. 42, 313–345.
Szabó, C.S., Harangi, S., Csontos, L., 1992. Review of neogene and quaternary volcanism of the Carpathian-Pannonian region. Tectonophysics 208, 243–256.
Szabó, C.S., Vaselli, O., Vannucci, R., Bottazzi, P., Ottolini, L., Coradossi, N., Kubovics, I., 1995. Ultramafic xenoliths from the Little Hungarian Plain (Western Hungary): a petrologic and geochemical study. Acta Vulcanol. 7, 249–263.
Szabó, C.S., Falus, G., Zajacz, Z., Kovács, I., Bali, E., 2004. Composition and evolution of lithosphere beneath the Carpathian–Pannonian Region: a review. Tectonophysics 393, 119–137.
Szabó, C., Hidas, K., Bali, E., Zajacz, Z., Kovács, I., Yang, K., Guzmics, T., Török, K., 2009. Melt–wall rock interaction in the mantle shown by silicate melt inclusions in peridotite xenoliths from the central Pannonian Basin (western Hungary). Isl. Arc 18, 375–400. https://doi.org/10.1111/j.1440-1738.2009.00672.x.
Tiepolo, M., Bottazzi, P., Foley, S.F., Oberti, R., Vannucci, R., Zanetti, A., 2001. Fractionation of Nb and Ta from Zr and Hf at mantle depths: the role of titanian pargasite and kaersutite. J. Petrol. 42, 221–232.
Van Orman, J.A., Grove, T.L., Shimizu, N., 2001. Rare earth element diffusion in diopside: influence of temperature, pressure, and ionic radius, and an elastic model for diffusion in silicates. Contrib. Mineral. Petrol. 141, 687–703.
Varas-Reus, M.I., Garrido, C.J., Marchesi, C., Bodinier, J.-L., Frets, E., Bosch, D., Tommasi, A., Hidas, K., Targuisti, K., 2016. Refertilization processes in the subcontinental lithospheric mantle: the record of the beni bousera orogenic peridotite (Rif Belt, Northern Morocco). J. Petrol. 57, 2251–2270.
Vaselli, O., Downes, H., Thirlwall, M.F., Dobosi, G., Coradossi, N., Seghedi, I., Szakács, A., Vannucci, R., 1995. Ultramafic xenoliths in Plio-Pleistocene alkali basalts from the eastern Transylvanian Basin: depleted mantle enriched by vein metasomatism. J. Petrol. 36, 23–53.
Vaselli, O., Downes, H., Thirlwall, M.F., Vannucci, R., Coradossi, N., 1996. Spinel-peridotite xenoliths from Kapfenstein (Graz Basin, Eastern Austria): a geochemical and petrological study. Mineral. Petrol. 57, 23–50.
Wang, C., Liang, Y., Xu, W., 2015. On the significance of temperatures derived from major element and REE based two-pyroxene thermometers for mantle xenoliths from the North China Craton. Lithos 224–225, 101–113.
Wilshire, H.G., 1987. A model of mantle metasomatism. Mantle Metasomatism Alkaline Magmat. Geol. Soc. Am. Spec. Pap. 215, 47–60.
Witt-Eickschen, G., Harte, B., 1994. Distribution of trace elements between amphibole and clinopyroxene from mantle peridotites of the Eifel (western Germany): an ion-microprobe study. Chem. Geol. 117, 235–250.
Witt-Eickschen, G., Seck, H., 1991. Solubility of Ca and Al in orthopyroxene from spinel peridotite: an improved version of an empirical geothermometer. Contrib. Mineral. Petrol. 106, 431–439.
Yao, L., Liang, Y., 2015. Closure temperature in cooling bi-mineralic systems: I. Definition and with application to REE-in-two-pyroxene thermometer. Geochim. Cosmochim. Acta 162, 137–150.
Zanetti, A., Vannucci, R., Bottazzi, P., Oberti, R., Ottolini, L., 1996. Infiltration metasomatism at Lherz as monitored by systematic ion-microprobe investigations close to a hornblendite vein. Chem. Geol. 134, 113–133.
Zanetti, A., Mazzucchelli, M., Rivalenti, G., Vannucci, R., 1999. The Finero phlogopite-peridotite massif: an example of subduction-related metasomatism. Contrib. Mineral. Petrol. 134, 107–122.